UNIVERSITY OF CALIFORNIA

Los Angeles

Empirical validation of optic nerve tethering by horizontal duction

A dissertation submitted in partial satisfaction

of the requirements for the degree Doctor of Philosophy in Mechanical Engineering

by

Seongjin Lim

2023

ABSTRACT OF THE DISSERTATION

Empirical validation of optic nerve tethering by horizontal duction

by

Seongjin Lim

Doctor of Philosophy in Mechanical Engineering

University of California, Los Angeles, 2023

Professor Joseph L. Demer, Co-Chair

Professor Vijay Gupta, Co-Chair

A hypothesis that the optic nerve and the optic nerve sheath pull the optic disc and its peripapillary regions is proposed and named “optic nerve tethering.” Although the optic nerve traction hypothesis seems reasonable, the empirical validation has not been conducted. Because empirical validation of the hypothesis is an essential step to develop this research field, I designed a set of four research projects for the purpose. Each project accounts for each different chapter in this dissertation.

Chapter 1 introduces background to understand optic nerve traction and its empirical validation. Because this dissertation requires multidisciplinary knowledge from ophthalmology, image processing, and continuum mechanics, the reader is recommended to read through materials in this introductory chapter.

In Chapter 2, a research project using scanning laser ophthalmoscopy was performed to take images on the optic disc and its peripapillary regions, while the eyes were fixing in various directions. By comparing images obtained in different eye positions, mechanical deformations were analyzed by computing two-dimensional strains. By presenting the strain values caused by eye rotation, the existence of mechanical deformations was demonstrated.

Chapter 3 explains a project using optical coherence tomography angiography for visualizing retinal blood vessels in 3D space. From volume changes in retinal blood vessels, the optic disc and its peripapillary regions were found to be pulled by the optic nerve, and the result was consistent with the optic nerve tethering hypothesis.

Chapter 4 introduces a magnetic resonance imaging study to analyze strains in the optic nerve resulting from eye rotation. In this project, the parameterization of optic nerve path obtained by magnetic resonance imaging was used to measure local optic nerve strains, which had never before been measured.

In Chapter 5, 3D digital image correlation and finite element method was employed to study adduction eye rotation. Scleral deformations from adduction were analyzed in two different ways, which validated and elaborated the optic nerve tethering hypothesis.

Chapter 6 concludes this dissertation and states open research questions for the optic nerve tethering hypothesis.

This dissertation of Seongjin Lim is approved.

Tom Chou

Dan Ruan

Vijay Gupta, Committee Co-Chair

Joseph L. Demer, Committee Co-Chair

University of California, Los Angeles

2023

DEDICATIONS:

To my parents and sisters, who have loved me.

To my friends, who have supported me.

To my coworkers, who have helped me.

TABLE OF CONTENTS

LIST OF FIGURES

2. Scanning Laser Ophthalmoscopy Demonstrates Disc and Peripapillary Strain During Horizontal Duction

3. Optical Coherence Tomography Angiography Demonstrates Strain and Volume Effects on Optic Disc and Peripapillary Vasculature Caused by Horizontal Duction

4. Validation and Quantification of Optic Nerve Strain Due to Horizontal Duction

5. 3D Digital Image Correlation Illustrates that Traction Force from Adduction is Transmitted to the Eyeball

LIST OF TABLES

5. 3D Digital Image Correlation Illustrates that Traction Force from Adduction is Transmitted to the Eyeball

ACKNOWLEDGEMENTS

I would like to express my gratitude to my advisor, Joseph L. Demer, who has guided me throughout my PhD program. I could see what a clinical scientist is as an example. Even after receiving this degree, I need to push myself forward to attain achievements. During the journey of my life, I may recall Dr. Demer from time to time.

I would like to acknowledge laboratory members. Changzoo Kim advised me a lot as a clinician and a mentor and sutured eyeballs for experiments. Chloe Lai lent her support like an older sister, and Dooseop Song was an excellent coworker for the creep experiment. Joseph Park helped me to adapt to this laboratory and learn medical knowledge in ophthalmology. Based on his work for a three-dimensional eye model, I could conduct finite element modeling. Somaye Jafari guided me to perform finite element analysis, and Stephanie S. Garcia took optical coherence tomography images and sutured eyeballs for experiments. Thanks to Nicolasa DeSalles and Yolanda McNair, I could concentrate on the research. Jose M. Gomez Godinez, a mechanician in the ophthalmology department, helped me to fabricate a mechanical system for digital image correlation experiment. With the members, I could make progress in the research.

VITA

EDUCATION

2015 B.S., Mechanical Engineering, Mathematics

Sungkyunkwan University, Seoul, South Korea

2019 M.S., Mechanical Engineering

Korea Advanced Institute of Science and Technology, Daejeon, South Korea

RESERCH EXPERIENCE

2016 – 2019 Research Assistant in Biomicrofluidics Laboratory
Korea Advanced Institute of Science and Technology, Daejeon, South Korea

2019 – 2020 Research Assistant in Nano-Bio Laboratory
National NanoFab Center, Daejeon, South Korea

2020 – 2023 Research Assistant in Ocular Motility Laboratory
University of California – Los Angeles, Los Angeles, CA

PUBLICATIONS

1. Kim S, Kim W, **Lim S**, Jeon JS. Vasculature-on-a-chip for in vitro disease models. *Bioengineering* 2017;4;8.

2. **Lim S**, Nam H, Jeon JS. Chemotaxis model for breast cancer cells based on signal/noise ratio. *Biophysical Journal* 2018;115;2034-2043.

3. Ryu J, Kim J, Oh J, **Lim S**, Sim SY, Jeon JS, No K, Park S, Hong S. Intrinsically stretchable multi-functional fiber with energy harvesting and strain sensing capability. *Nano Energy* 2019;55;348-353.

4. Shin Y, **Lim S**, Kim J, Jeon JS, Yoo H, Gweon B. Emulating endothelial dysfunction by implementing an early atherosclerotic microenvironment within a microfluidic chip. *Lab on a Chip* 2019;19;3664-3677.

5. Park S, **Lim S**, Siriviriyakul P, Jeon JS. Three-dimensional pore network characterization of reconstructed extracellular matrix. *Physical Review E* 2020;101;052414.

6. Song Y, **Lim S**, Kim YT, Park YM, Jo DA, Bae NH, Lee SJ, Choi BG, Im SG, Kim HU, Lee KG. Deep learning enables accurate analysis of images generated from droplet-based digital polymerase chain reaction (dPCR). *Sensors and Actuators B: Chemical* 2023;379;133241.

7. Song D, **Lim S**, Park J, Demer JL. Linear viscoelasticity of human sclera and posterior ocular tissues during tensile creep. *Journal of Biomechanics* 2023;151;111530.

8. **Lim S**, Tran A, Garcia SS, Demer JL. Optical coherence tomography angiography demonstrates strain and volume effects on optic disk and peripapillary vasculature caused by horizontal duction. *Current Eye Research* 2023;48;518-527.

9. Quresh A, **Lim S**, Suh SY, Mutawak B, Chitnis PV, DemerJL, Wei Q. Deep-learning-based-segmentation of extraocular muscles from magnetic resonance images. *Bioengineering* 2023;10;699.

10. Park J, Moon S, **Lim S**, Demer JL. Scanning laser ophthalmoscopy demonstrates disc and peripapillary strain. *American Journal of Ophthalmology* 2023;254;114-117.

11. **Lim S**, Demer JL. Empirical quantification of optic nerve strain due to horizontal duction. *Bioengineering* 2023;10;931.

CHAPTER 1. INTRODUCTION

1.1. Prologue

During the past few decades, biomechanics in the ophthalmology field have progressively developed and elucidated many scientific findings[1, 2]. Because mechanical forces and deformations can be related to pathophysiology for ophthalmic disorders[2], researchers have investigated biomechanical phenomena of cornea[3, 4], iris[5], lamina cribrosa[6, 7], and sclera[8, 9]. However, even researchers in ocular biomechanics have paid scant attention to biomechanical effects of eye movement[10]. The eye rotates within a range of up to 55°[11], and saccades occur three times per a second[12]. Given the dynamic motility of the eye, reappraisal of relations between eye movement and ocular biomechanics is necessary.

Magnetic resonance imaging demonstrated that horizontal rotation towards the midline (adduction) renders the optic nerve and its sheath taut, stretching them[10]. The adducted, taut optic nerve and its sheath were presumed to transfer mechanical loads to the optic disc and peripapillary region; this phenomenon regarding this hypothesis has been named "optic nerve tethering." Researchers have used imaging[10, 13, 14] and finite element analysis[15, 16] to investigate this biomechanical phenomenon. Representative imaging techniques that have been used for this purpose are scanning laser ophthalmoscopy[14], optical coherence tomography[13], and magnetic resonance imaging[10].

Though imaging supported the hypothesis of optic nerve tethering, optic nerve tethering has not been validated directly. Previous empirical studies also measured deformations of retinal layers[13, 14] and the optic nerve[17, 18], but the disparate evidence had not been linked to explain the optic nerve tethering in terms of continuum mechanics. Moreover, because numerical simulation

uses a computational model to simplify the biological environment, results from the numerical simulation cannot definitively prove the hypothesis. As a result, the hypothesis for optic nerve tethering has been controversial among researchers. To address the problem, a set of research experiments was designed and conducted.

The principal question in this dissertation is whether optic nerve tethering can be verified and quantified via image processing. To answer the main question, I decomposed the research question into several pieces. Thus, the first task was to investigate if mechanical deformations due to eye rotation exist. The second task was to study whether the deformations are due to traction force, and the next question was about the source of the traction force. The last question in this project was about whether the traction force can be significantly transferred to the eyeball. By resolving each question, I tried to find an answer to the main question for the dissertation.

1.2. Preliminaries

Before exploring this question, a few preliminaries are to be introduced. Since this multidisciplinary research topic lies in the intersection of ophthalmology, continuum mechanics, and image processing, I explain the three domains briefly in this introductory chapter. First, I define the anatomical terminology used in this dissertation. Then, I will present continuum mechanics and image processing sequentially. Lastly, I will introduce statistical methods used in this dissertation.

1.2.1. Posterior segment of the eye

The **optic nerve** is a primary region of interest in the optic nerve traction hypothesis. Because the optic nerve inserts on the posterior eye, resultant effects of the optic nerve traction would influence on the posterior segment. Therefore, I introduce anatomical features in the posterior segment that are important to designing the research.

The **optic nerve** is a cranial nerve that transmits the visual signal from the retina to the brain. Considering the fact that axons of the optic nerve account for 38% of axons in the central nervous system[19], the optic nerve is an important sensory system in the human body. The optic nerve can be considered as having four anatomical sections: the intraocular, the intraorbital, the intracanalicular, and intracranial segments[19]. Throughout this dissertation, optic nerve usually refers to the intraocular and intraorbital segments. The very short intraocular segment is situated in the globe, and the intraorbital segment runs from the posterior region of the globe to the orbital apex. At the end of the intraorbital segment, the dura of the optic nerve is fixed to the bone[19] and surrounded by Annulus of Zinn, which is tendinous origin of extraocular rectus muscles[20].

The **optic disc**, also known as optic nerve head, is a spot on the retina where the axons of the retinal ganglion cells converge and the retinal vessels originate[21]. The optic disc includes the **lamina cribrosa** that is a mesh-like structure to supply structural support to the retinal ganglion cell axons[22, 23]. Damage to the lamina cribrosa is postulated to initiate ophthalmic disorders[24], and the lamina cribrosa is known to be sensitive to mechanical stimuli[25]. Therefore, mechanical deformations of the optic disc may have a potential to induce pathological changes in the eye. Since intraocular pressure changes have been primarily postulated as the mechanism of the mechanical stimuli for the lamina cribrosa[26, 27], the possibility of deformations due to eye rotation also needs to be investigated (**Chapter 2**).

The **sclera** is the outer layer of the eyeball, and it plays an important structural role in protecting internal layers of the eye[9]. Because the sclera is exposed to continuous mechanical stimuli due to eye movement and fluctuating intraocular pressure[9], its resilience and resistance are critical to all functions of the eye.

1.2.2. Continuum mechanics

Strain represents how much an object deforms locally[28], and Green-Lagrangian strain tensor is used to quantify strain in this dissertation. Because strain is a second-rank tensor, von Mises strain[29] is also used to represent deformation as a scalar. **Stress** is a second-rank tensor to describe how large force acts in a local region of an object[28]. Stress is a criterion for changes in mechanical behavior or fracture in a solid[30, 31], including biological tissues[32, 33]. Moreover, strain and stress are closely related, and hence strain is an important quantity throughout this dissertation.

Finite element method is a numerical technique designed for solving discretized partial differential equations[34]. Since the governing equations in solid mechanics are partial differential equations[28], finite element method is also used in ocular biomechanics[35]. In this approach, a complex domain is subdivided into small parts called finite elements, and physical fields are approximated on these discretized finite elements. Physical equations are formulated for each finite element, and the resulting equations are assembled across the entire domain using nodal connectivity. Following the assembly, a global equation is formed, and boundary conditions are imposed. Subsequently, a numerical solution for the global equation is obtained[36]. This computational approach was utilized to simulate deformations of eyes under loadings in **Chapter 5**.

1.2.3. Image processing

There are many modalities for clinical imaging of the eye[37, 38]. In this dissertation, confocal scanning laser ophthalmoscopy (**Chapter 2**), optical coherence tomography, optical coherence tomography angiography (**Chapter 3**), and magnetic resonance imaging (**Chapter 4**) were used for *in vivo* imaging. In addition, digital single-lens reflex cameras were used to take optical images during the *ex vivo* study (**Chapter 5**). In order to quantitatively measure mechanical deformations, image processing algorithms were applied to the images. For the understanding, I will describe terms in image science tersely.

Image registration refers to a transformation that maps one image to one another. The reference and referred image can come from different times, different devices, and different angles[39]. For the measurement of mechanical deformations, the images need to have a same coordinate system. Therefore, image registration is important in many applications.

Image segmentation is the process of identifying a set of pixels to represent a certain type of an object. The image segmentation is an essential technique for computer vision, and it is used for a variety of applications such as medical image analysis and video surveillance[40]. Although numerous rule-based algorithms have been developed, the latest studies converge to deep learning based image segmentation[40]. The deep learning network extracts features from large scale data by imitating the learning process of a human being[41]. There are several types of deep learning networks, and the convolutional neural network is the most representative structure. In a convolutional neural network, filters representing receptors are convolved across the input data,

and the filters are driven by activation functions to simulate neurotransmission[42]. In this dissertation, a convolutional neural network was trained for image segmentation.

Optical flow is an algorithm to estimate motion of an object by comparing sequential images. Though conventional optical flow algorithms usually used partial derivatives of the image intensity, current studies on optical flow converge to deep learning based algorithms[43]. This shift by the deep learning age results in accuracy improvements as well as reduced computation time[43, 44].

Digital image correlation is an image-based technique for measuring full-field deformation[45]. Speckle patterns are deposited on the surface of an object, and changes in the patterns are used to track deformation of the object. By computing cross correlations among image subsets from sequential images, deformations can be measured accurately. This algorithm is continuously evolving towards the fully automated and faster computation[45]. The seed points and window sizes are manually determined for the conventional digital image correlation algorithm[45]. Due to the considerable computational time required by the algorithm, the use of a convolutional neural network for digital image correlation has also been suggested[46]. In this dissertation, scleral deformation was measured by a conventional 3D digital image correlation algorithm[47] (**Chapter 5**).

1.2.4. Statistical methods

The **t-test** is a parametric statistical method used to compare means between two distinct groups, determining whether their means differ significantly[48]. As the experimental subjects in this dissertation were not divided into two separate groups, a paired t-test was employed. This test

assumes normal distributions with equal variance and independence. In cases where the samples do not satisfy the normality assumption, the **Wilcoxon test** was used.

The analysis of variance (**ANOVA**) is a parametric technique to test if means of three or more groups differ significantly. Depending on the number of factors influencing a dependent variable, either one-way ANOVA or two-way ANOVA were employed. ANOVA assumes normal distributions with equal variance and independence. Additionally, it assumes that the impact of different factors on the dependent variable is a linear combination of the individual effect of each factor. In cases where these assumptions are violated, the **Friedman test** was used.

The **generalized estimating equation** method is employed to estimate parameters for correlated observations, and the regression parameters are estimated by the following estimating equation[49].

$$\sum_{i=1}^{N} \frac{\partial \mu_i}{\partial \beta} V_i^{-1} \{Y_i - \mu_i(\beta)\} = 0 \qquad (1)$$

where N, β, Y_i, μ_i, and V_i are the number of subjects, the regression parameters, the measurement of the i-th subject, the expectation of Y_i, and the estimated covariance matrix of Y_i. Generalized estimating equations captures the relationships between predictor variables and the response variable. This method can adjust the level of significance for possible correlation between, for example, the two eyes of the same subject, and has type 1 error characteristics superior to t-testing[50].

Chapter 2. Scanning Laser Ophthalmoscopy Demonstrates Disc and Peripapillary Strain During Horizontal Duction

Publications included in this chapter:

Park J, Moon S, **Lim S**, Demer JL. Scanning laser ophthalmoscopy demonstrates disc and peripapillary strain during horizontal eye rotation in adults. *American Journal of Ophthalmology* 2023;254;114-117.

As the introduction explains, previous studies postulated that the optic nerve tethering indeed occurs in large angle adduction[10, 51]. Although straightening of the optic nerve path was clearly seen by magnetic resonance imaging[10], the straight optic nerve path does not confirm the hypothesis that the optic disc and peripapillary regions are deformed by eye rotation. In fact, if the optic nerve and its dura are much softer than the sclera, traction on the optic nerve might not affect the sclera. Therefore, scanning laser ophthalmoscopy was used to observe deformations of the optic disc[14]. The optic disc was supposed the likely region where the force by eye rotation is concentrated (Fig. 1). Because a force on any imperfect object is concentrated on a cavity or an imperfection, this idea is plausible from the perspective of mechanics. Moreover, the optic disc is an anatomically important region for axons of the retinal ganglion cells to transverse the sclera. As a result, the scanning laser ophthalmoscopy was used to observe the optic disc, while an eye was fixated at an eccentric position (Fig. 2).

Although two-dimensional images from scanning laser ophthalmoscopy were used to measure displacements of the blood vessels in previous studies[14], there was no fixed marker as a

position reference in repeated scanning laser ophthalmoscopy images, so obtained displacement values are local rather than global displacements. As a result, displacement data are highly dependent on the registration process. Because image registration and tracking of the retinal vessels were performed manually in a prior study[14], analysis might not have been fully reliable.

In addition, displacements cannot provide the information on deformations because the eye rotates. As a result, this project was planned to ascertain how the optic disc and peripapillary region deform after eye rotation.

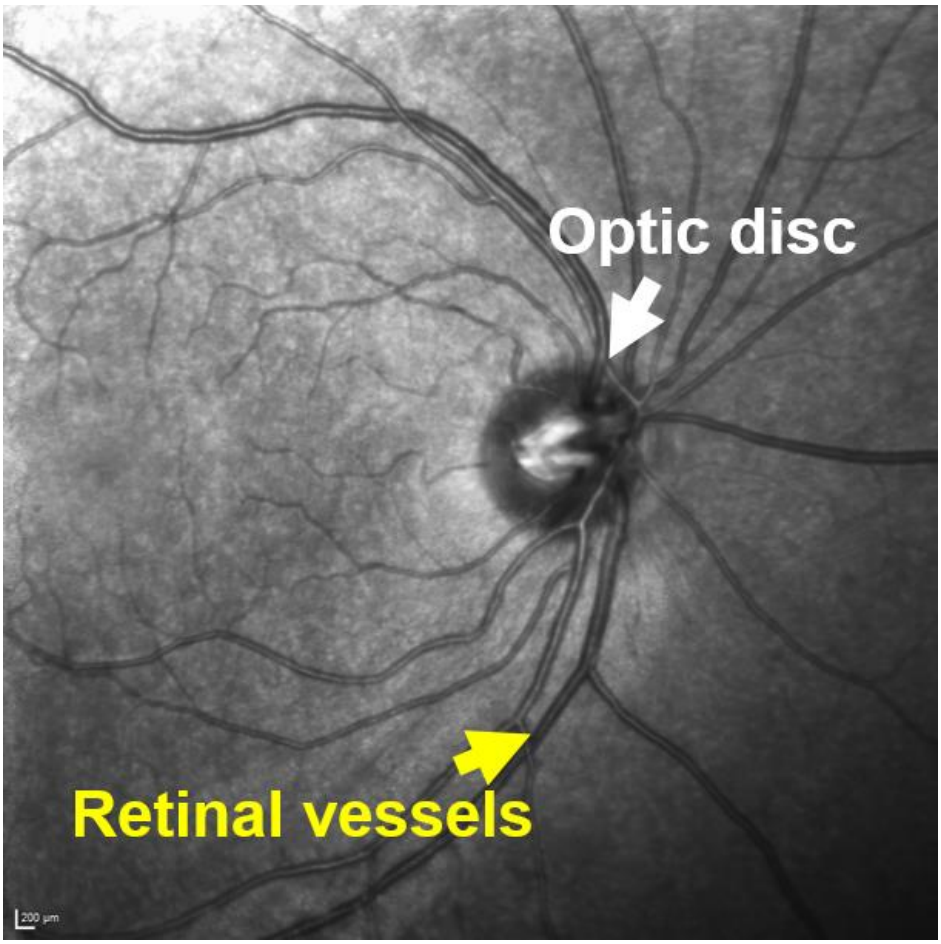

Figure 1. Scanning laser ophthalmoscopy images for an optic disc and retinal vessels.

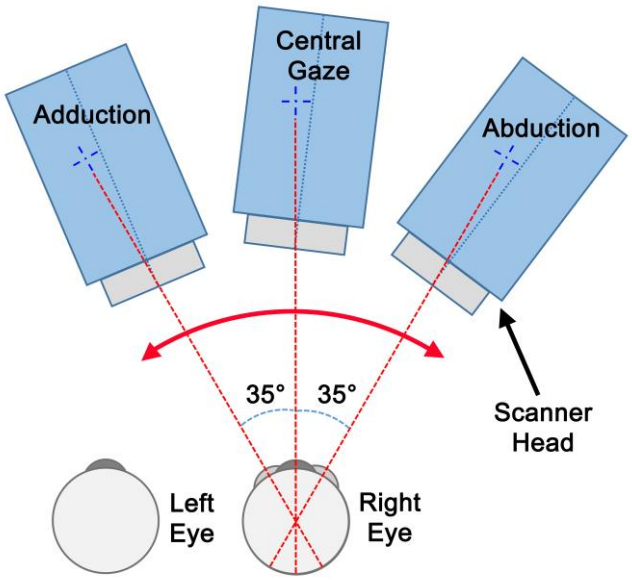

Figure 2. A diagram to illustrate an experiment protocol. The eye and imager are rotated by the same angle.

This project followed a protocol approved by the Institutional Review Board of the University of California Los Angeles that conforms to tenets of the Declaration of Helsinki. Healthy adults (mean ± SD, 26 ± 5 years; 10 men and 12 women) were recruited for subjects, and they gave the written informed consent before the participation. Scanning laser ophthalmoscopy images were taken by using a commercial imager (Spectralis, Heidelberg Engineering, Heidelberg, Germany). The images covered an area of 8.9 × 8.9 mm^2, and image resolution was about 11.6 μm. The eye positions were fixed at the central gaze, 35° adduction, and 35° abduction, while the head was fixed. The imager was rotated by referring to a goniometer, and imaging was performed for each eye position.

To automate the analysis process, raw images typically having imbalanced brightness were preprocessed for illumination correction. A background image was generated by using a morphological opening with a 59×59 circular shaped kernel. The logarithmic value of the

background image was subtracted from the logarithmic value of the raw image. To avoid the singularity from the logarithmic function, one was added to the image values. Then the brightness was adjusted by normalizing the scale to the minima and maxima of resultant images. Torsion of the retina was corrected by rotating the image by an amount of the offset. Then image registration between different eye positions was conducted by speed-up robust features[52], and a deep neural network[53] was used for identifying the blood vessels. Displacements of the blood vessels were computed by deep learning based optical flow[43], and the displacements were converted to strains. Because strains were used instead of displacements, the deformation quantities were decoupled from a coordinate system, and independent of optical magnification. The overall process is depicted in Figure 3.

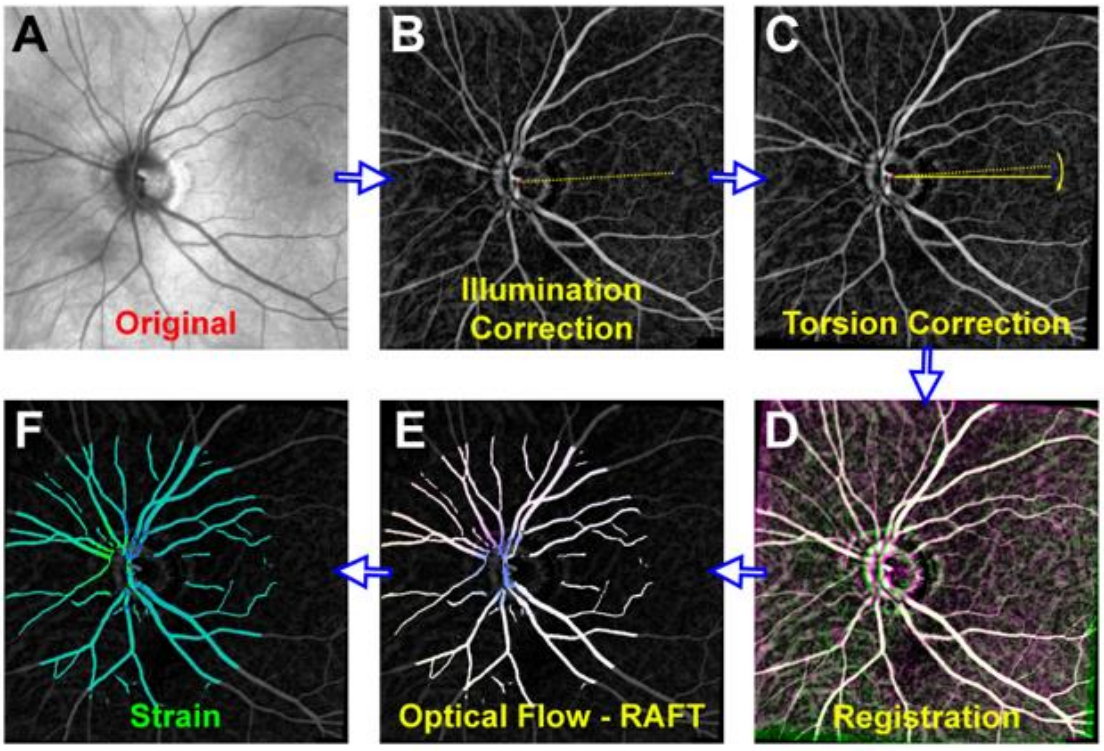

Figure 3. Workflow to analyze scanning laser ophthalmoscopy images for the measurements of strains on retinal vessels after eye rotation.

Since only retinal blood vessels are regions of interest, precise and automatic identification of retinal vessels was essential. To use a convolutional neural network[53] for image segmentation, 100 scanning laser ophthalmoscopy images and corresponding manual masks of the vessels were prepared (Fig. 4). The dataset was augmented by using a variety of methods because the data augmentation improves the performance of a deep neural network[54]. In this study, the dataset was augmented by using the elastic deformation[55], and then online augmentation was applied for each training batch by using the image rotation, flipping, noise addition, and gamma correction (Fig. 5). The parameters for the noise addition and gamma correction were randomly chosen. The quality of the image segmentation for a scanning laser ophthalmoscopy image is illustrated in Figure 6 The tested image was not included in the training dataset.

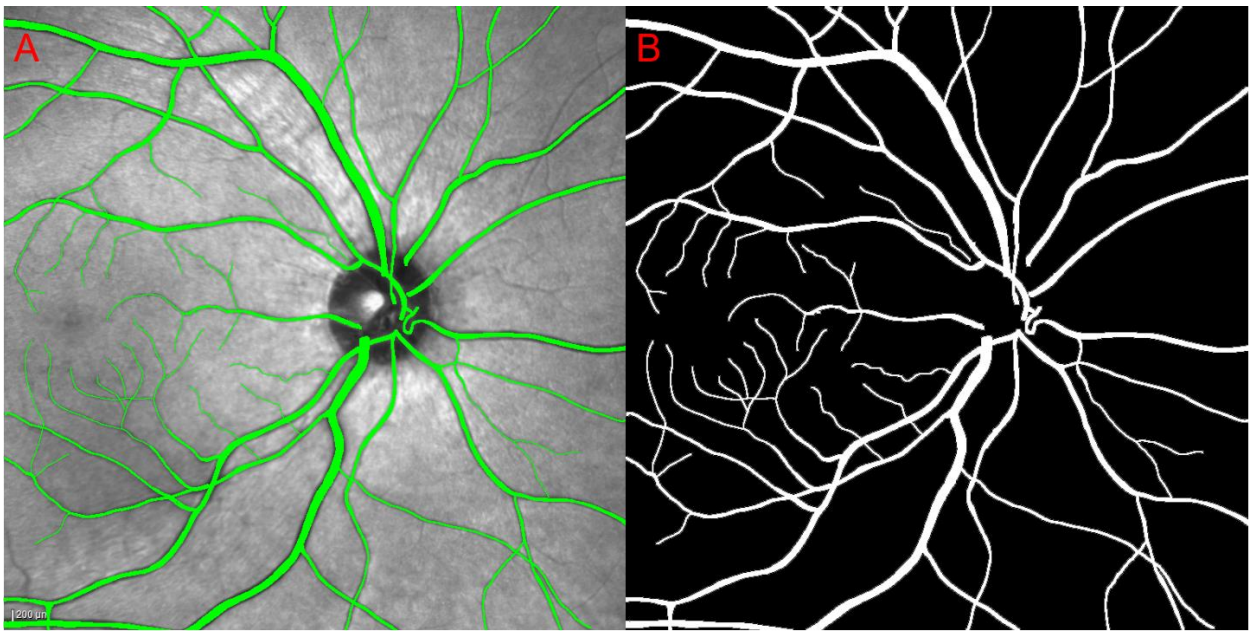

Figure 4. An example of a manually generated mask and its binarized output for retinal blood vessels. The binarized masks were used to train the convolutional neural network.

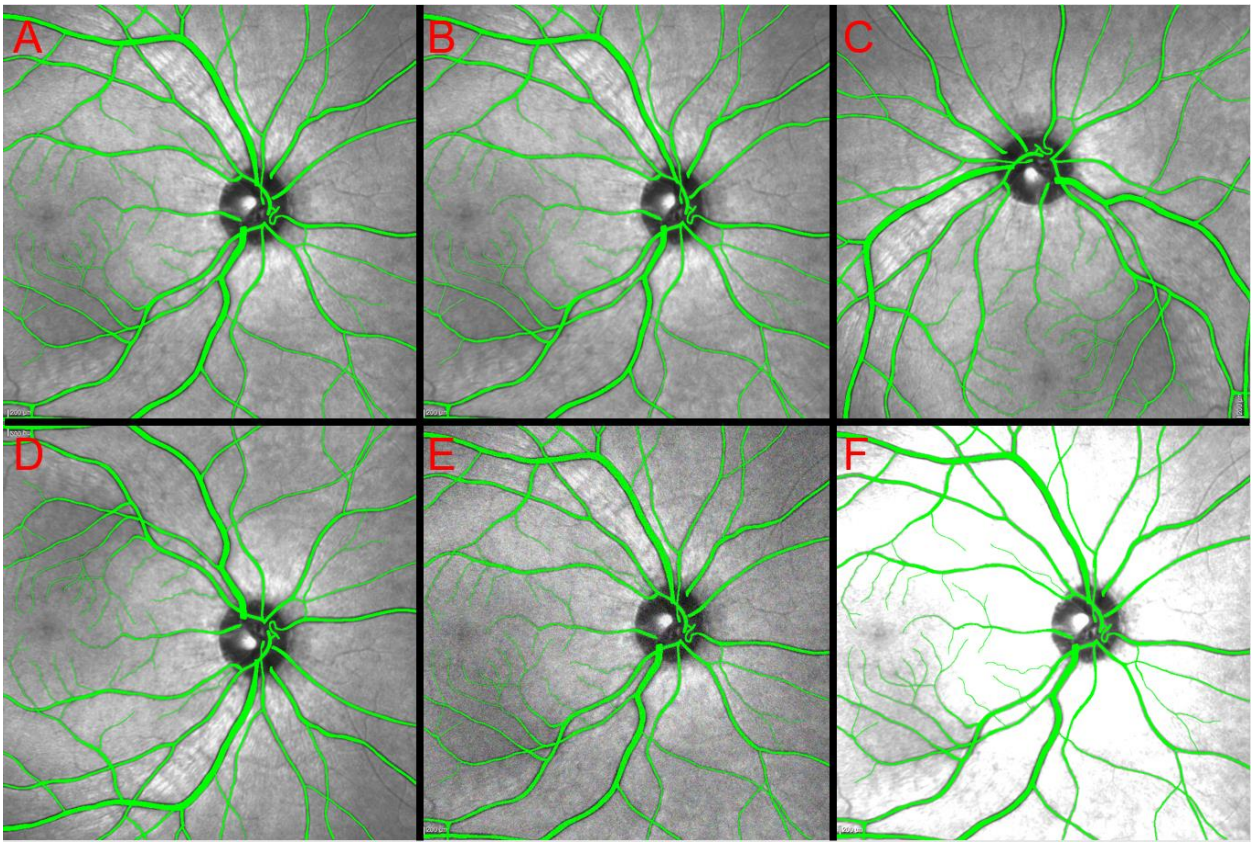

Figure 5. Data augmentation for improving the performance of the deep neural network. (A) The original image. (B) Elastically distorted image. (C) Rotated image. (D) Vertically flipped image. (E) The image with addition of Gaussian white noise. (F) The image with gamma correction.

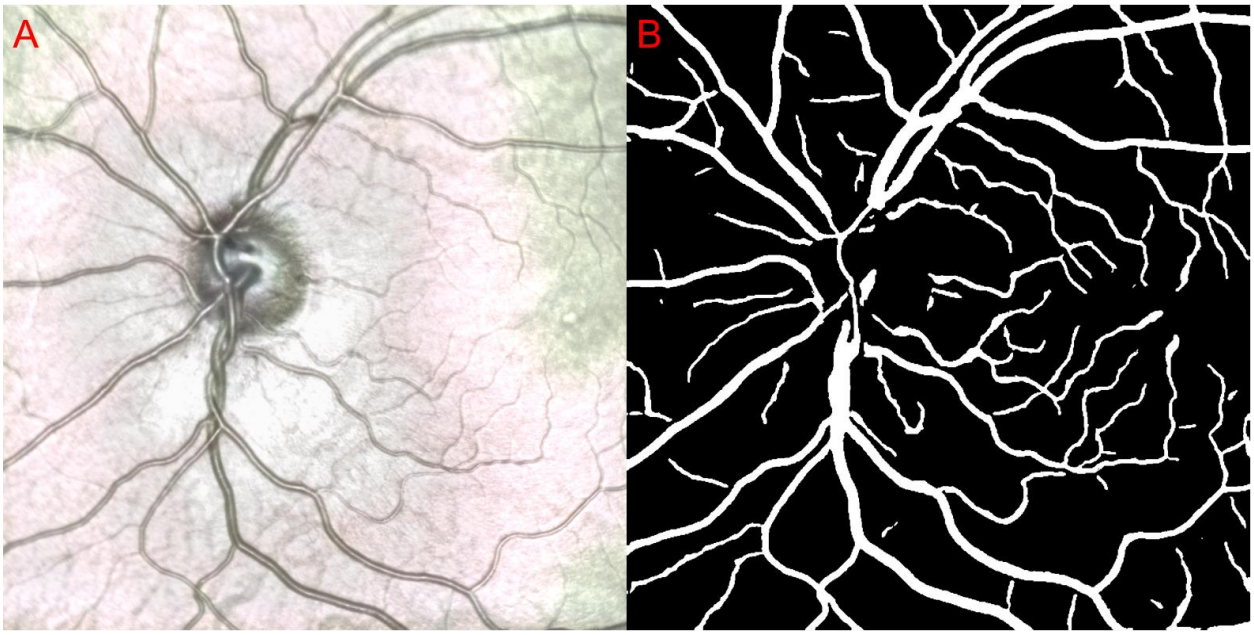

Figure 6. The segmentation result from the trained deep neural network. The tested image was not included in the training dataset.

For the analysis of the strains on retinal vessels, domains were segmented into 8 regions depending on relative positions with respect to the center of the optic disc.

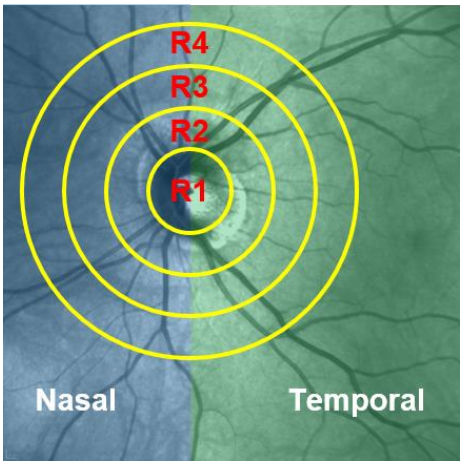

Figure 7. The divided regions depending on relative positions with respect to the optic disc. Region size is equal to disc radius.

The repeatability of the imaging and analysis was confirmed by comparing supplicate pairs of images obtained the same eye positions for eye 20 eyes of 10 normal adults.

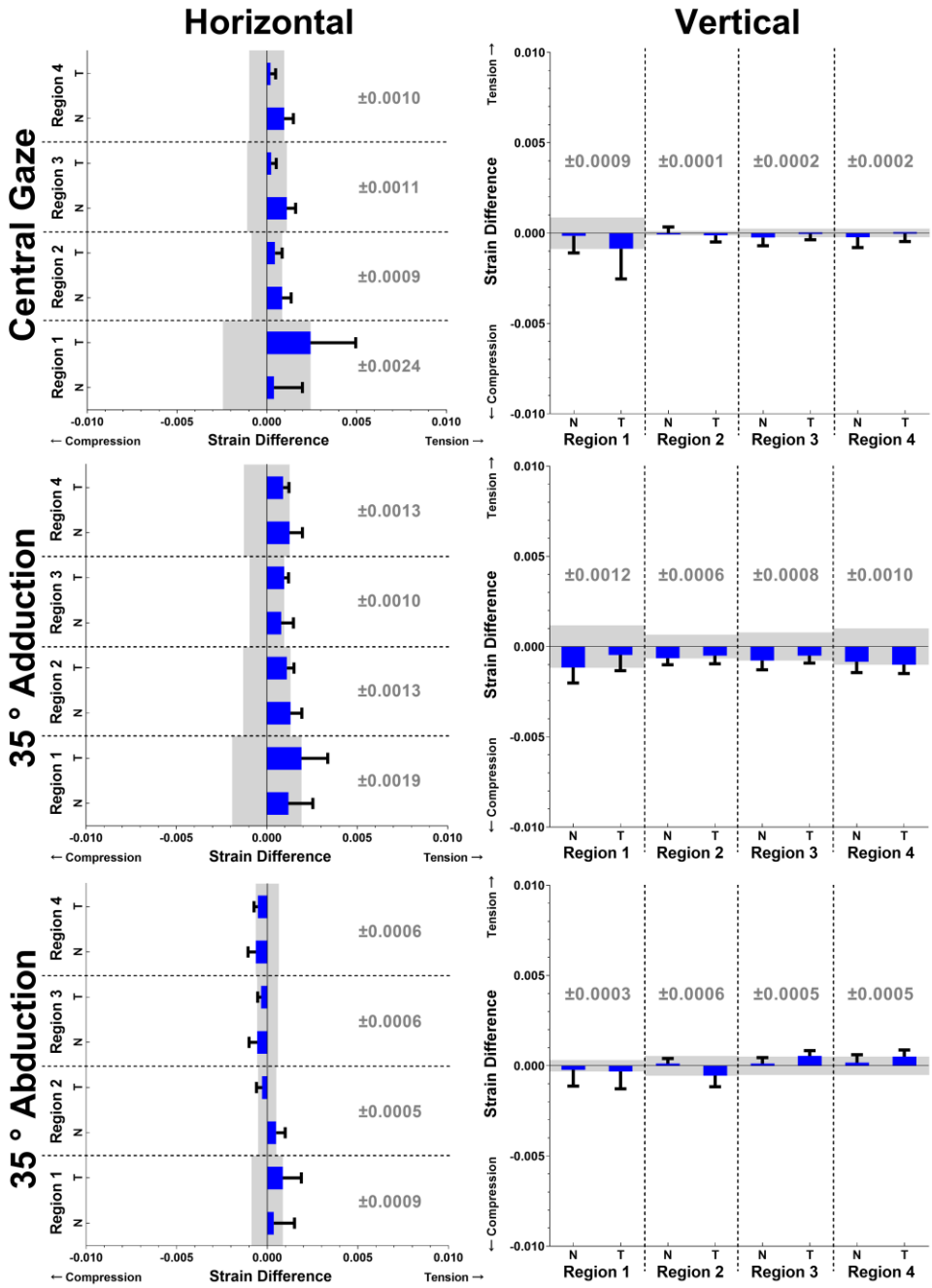

Figure 8. Repeatability test horizontal and vertical strains. Imaging was performed twice in the same eyes in a single imaging session. The error bars represent standard errors.

After confirming that the experimental process is repeatable, strains from eye rotation were analyzed. Significant horizontal strains were observed within, and to a lesser extend in regions adjacent to the optic disc, more in adduction than abduction (Region 1 in Fig. 7). The strains were concentrated at the optic disc and decreased with the distance from the optic disc. Moreover, nasal regions exhibited significantly larger strains than temporal regions in adduction. On the other hand, vertical strains were much smaller than horizontal strains in both cases.

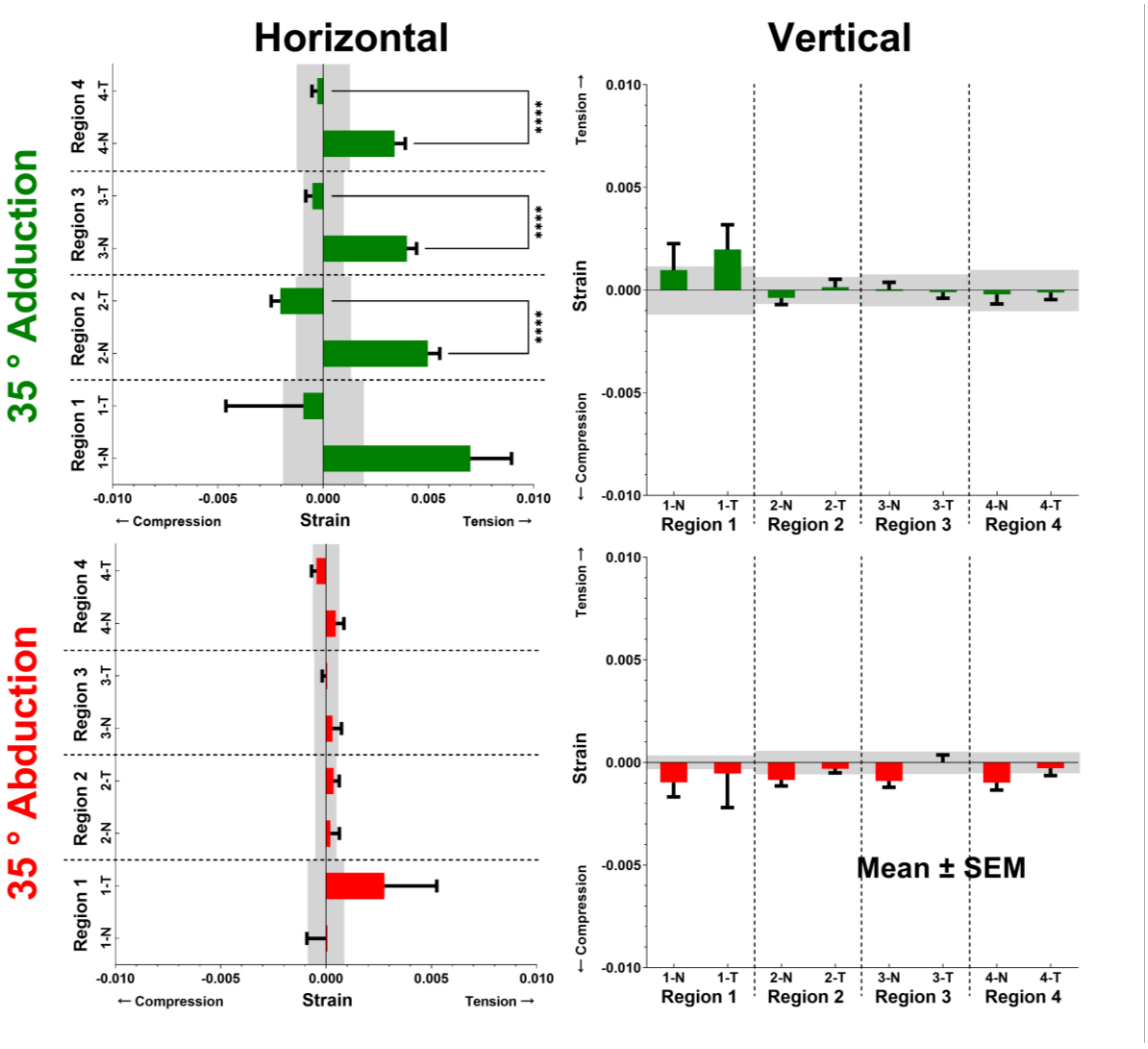

Figure 9. Horizontal and vertical strains for 35° adduction and abduction. The error bars represent standard errors, and the sample size was 44 eyes of 22 normal adults.

This research supported the statement that the optic disc and its peripapillary regions deform by eye rotation. Strain analysis provided the geometric information on whether the tissue was under the expansion or the compression. Thus, the retinal blood vessels were found to be expanded or compressed depending on regions. Although many research questions remain, the existence of mechanical deformations of retinal tissues induced by the eye rotation was confirmed. In the past, eye rotation was thought to be associated only with phenomena only involving extraocular muscles and extraocular tissues. Because this project linked the eye movement to internal ocular biomechanics, this study has opened an avenue to interpretation of ocular biomechanics related to eye movement.

CHAPTER 3. Optical Coherence Tomography Angiography Demonstrates Strain and Volume Effects on Optic Disc and Peripapillary Vasculature Caused by Horizontal Duction

Publications included in this chapter:

Lim S, Tran A, Garcia SS, Demer JL. Optical coherence tomography angiography demonstrates strain and volume effects on optic disk and peripapillary vasculature caused by horizontal duction. *Current Eye Research* 2023;48;518-527.

The scanning laser ophthalmoscopy study in the previous chapter demonstrated that horizontal duction induces mechanical deformation in the optic disc and retina. However, whether such deformation arises from traction by the optic nerve was not demonstrated with certainty from such data. For example, he optic disc and its peripapillary regions could be pulled or alternatively pushed by the optic nerve. Even were the optic nerve to push against the optic disc, resulting mechanical deformations on the optic disc and its peripapillary regions could be observed by scanning laser ophthalmoscopy. To determine the direction of the driving force, I investigated 3D strains and volume changes of blood vessels during horizontal duction.

Optical coherence tomography angiography performs repeated volumetric imaging at high speed in the same retinal area, and the decorrelation between sequential images generates motion contrast[56]. Because signal decorrelation from flowing erythrocytes in retinal blood vessels are detected, the 3D microvasculature is visualized. In this study, ten normal adults (mean ± standard deviation, 37 ± 15 years; five men and five women) were imaged by using a commercial optical coherent tomography scanner with angiographic function (Spectralis, Heidelberg Engineering,

Heidelberg, Germany). The subjects consented to a protocol approved by the University of California, Los Angeles Institutional Review Board conforming to the tenets of the Declaration of Helsinki. Eye position was fixed at the central gaze, 30° adduction, and 30° abduction. Structural optical coherence tomography images were also obtained over a region of 9×7.5 mm^2 centered on the optic disc, and the optical coherence tomography angiography images spanned a 3×3 mm^2 centered on the optic disc.

Due to its working principle of local decorrelation as the vascular indicator, numerous repeated scans are necessary for optical coherence tomography angiography. Thus, for optical coherence tomography angiography, a narrow field of view was used to reduce imaging time. To compensate for limitation in anatomical orientation landmarks due to the narrow field of view, a combination of optical coherence tomography angiography and structural optical coherence tomography was used. Also, although digital volume correlation[57] is a conventional method for measuring strains by comparing single pairs of images, the algorithm was not appropriate for this project. Because I used optical coherence tomography angiography and optical coherence tomography for two different eye positions, I used two pairs of two modes of images. Therefore, I developed a method based on 3D scale-invariant feature transform[58]. The 3D scale-invariant feature transform extracted feature points that were common between different images, and I used point-set registration[59] for the extracted feature points in order to register the images.

Then the registration process generated mathematical relations between two arbitrary images. For feature points F_1 and F_2 from a pair of images, the relationship of one feature point to another one can be approximated by a matrix expression: $F_2 \cong sRF_1+T$ where R represents a rotation matrix, s is a scale factor, and T indicates translation. Three mathematical relations for the pairwise registration were obtained from a pair of angiogram and structural tomogram images obtained in

primary gaze, a pair of structural tomograms obtained in primary gaze and ab- or adduction, and a pair of angiogram and structural tomogram images obtained in horizontal duction. Sequential uses of the mathematical expressions for the primary gaze optical coherence tomography angiography images enabled me to register them to optical coherence tomography angiography images in ab- or adduction. Since retinal vessels were identified by a convolutional neural network[53], and the vessels were embedded in the structure, the displacements of the retinal vessels could be computed. From the displacement, strains could be calculated by following the formula. $E = \frac{1}{2}\left((\nabla u)^T + (\nabla u) + (\nabla u)^T \cdot (\nabla u)\right)$ where ∇u and ∇u^T represent the displacement gradients and their transposes. Green-Lagrange strain E is related to the right Cauchy tensor C=2E+I where I is the identity matrix. The square root of the determinant of C represents the relative volume after the deformation.

Because ocular torsion is individually variable and also changes with gaze direction according to Listing's Law[60], I standardized image orientation in a coordinate system based on anatomical landmarks identified in wide field imaging. The Bruch's membrane opening centroid was used as the origin of the coordinate system. Using the stack of wide field B-scan optical coherence tomography images to obtain a volumetric reconstruction, a plane was fitted to the Bruch's membrane opening using random sample consensus[61], which is a robust method minimally affected by outliers. The normal vector of the Bruch's membrane opening plane defined the Z-axis, with the anterior direction positive. Next, the fovea was located in the volumetric optical coherence tomography by applying a derivative test for the identified retinal surface to find a local minimum that corresponds to the bottom of the foveal pit. Then the X-axis was defined by the line from the Bruch's membrane opening center to the fovea, with temporal direction positive. The Y-axis was defined by the cross-product of the Z- and X-axes, and thus is perpendicular to

both. A standard 3-dimensional Cartesian coordinate system was thus defined for each eye that could then be applied to high resolution optical coherence tomography angiography (Fig. 10B).

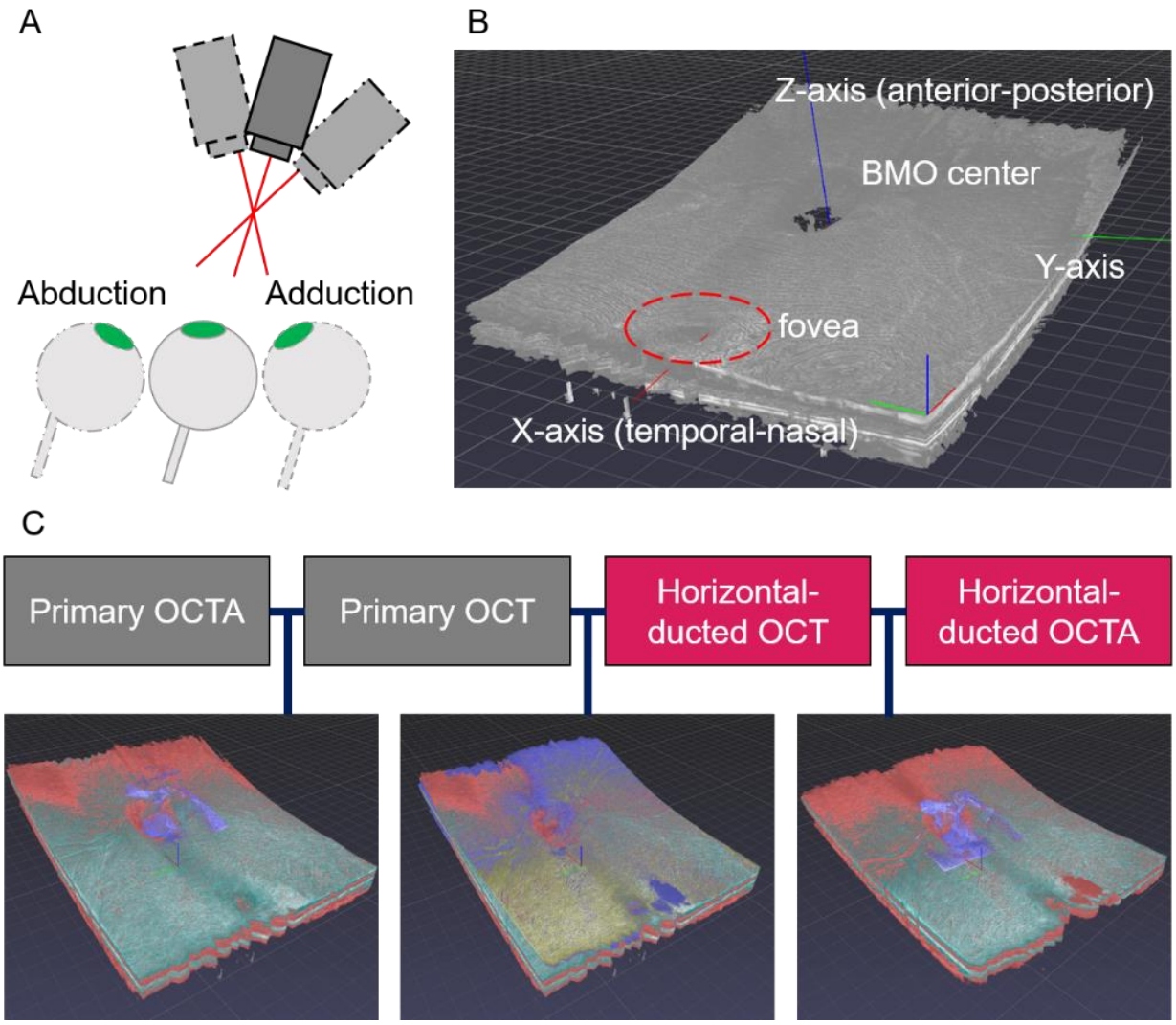

Figure 10. Analysis workflow to analyze effects of the eye rotation. (A) Optical coherence tomography angiography images in multiple gaze positions were obtained by rotating the scanner along in coordination with the eye. (B) A local coordinate system was defined in relation to the Bruch's membrane opening and fovea. (C) Pairs of images are registered by 3D scale-invariant feature transform and point-set registration, and three matrix expressions for the registration are computed.

I investigated repeatability of imaging and analysis of von Mises strains and relative vascular volumes. Ideally, for pairs of images obtained in the same eye positions, von Mises strain should be zero, and relative volume should be unity. Observed von Mises strains for repeated central gaze, adduction, and abduction were 0.0026 ± 0.0019 (mean ± standard deviation), 0.0021 ± 0.0014, and 0.0017 ± 0.0012, respectively. On the other hand, von Mises strain relative to central gaze was 0.028 ± 0.010 both in adduction and 0.029 ± 0.024 for abduction ($P < 0.02$ for each). Eta correlation analysis demonstrates that eye rotation induces significant strains, compared to the same gaze positions (correlation coefficient = 0.766, strong association).

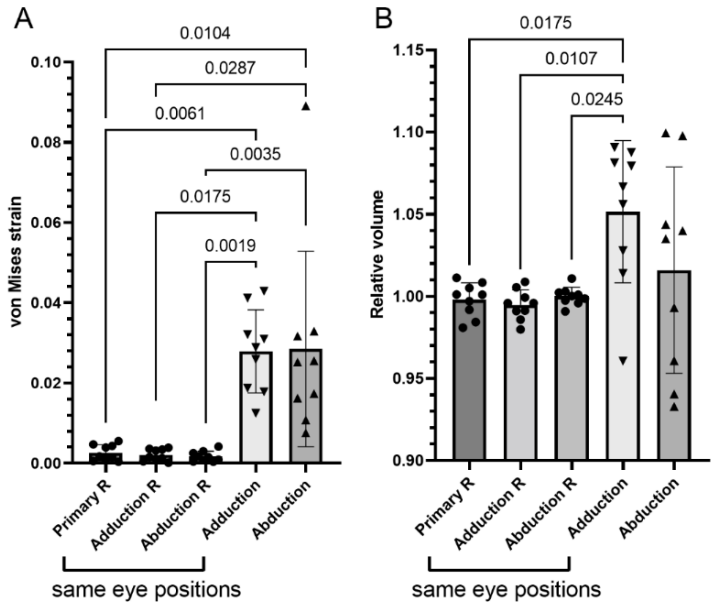

Figure 11. Repeatability and effect of horizontal duction in 9 eyes of 5 adults. Each symbol represents one eye. (A) von Mises strain. (B) Relative vascular volume. Left three columns depict changes on repeated imaging in identical eye positions in each individual, and right two columns show effects of horizontal duction. Note strains due to duction (A) far exceed repeatability, as does the significant volume increase in adduction but not abduction. For statistical analysis, the Friedman test (A) and one-way ANOVA (B) were used. Error bars are standard deviations.

I also examined the effect of duction on relative vascular volume (Fig. 11B). Without any change, the relative volume should remain unity. Indeed, when repeatability testing was performed in the same eye positions in the same eyes for central gaze, adduction, and abduction, relative values were 0.998 ± 0.010, 0.995 ± 0.009, and 1.000 ± 0.005, respectively, all statistically indistinguishable from unity (P > 0.128, 2-tailed t-test). This finding confirms that vascular volume measurement is repeatable, which was also the case for abduction in which relative volume at 1.016 ± 0.059 was also statistically indistinguishable from unity (P = 0.468). However, in adduction vascular volume increased significantly by over 5% to a relative volume of 1.052 ± 0.041 (P = 0.007).

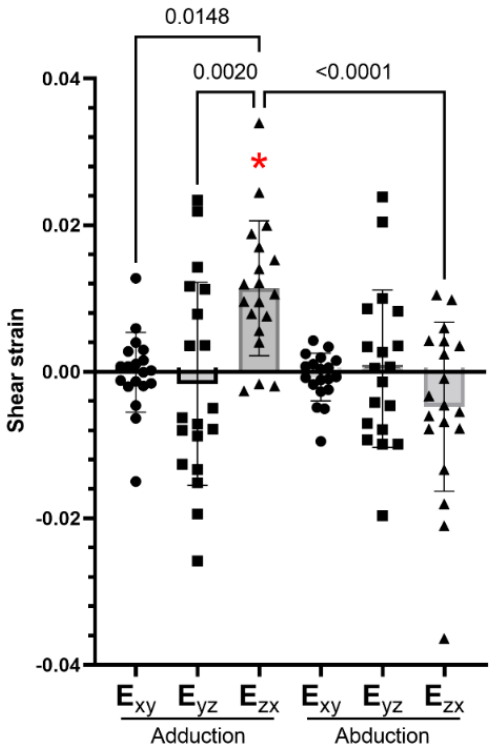

Figure 12. Shear strains induced by horizontal duction, in coordinate system defined in Fig. 10. Each symbol represents one of the 19 individual eyes. The Friedman test was used, and the asterisk represents data that is significantly different from zero. Error bars are standard deviations.

I also measured shear strains associated with horizontal duction that are defined in the three orthogonal planes that include a pair of coordinate axes defined in Fig. 10. In adduction, positive and negative shear strains E_{XY} and E_{YZ} were symmetrically distributed so that their averages did not differ significantly from zero ($P > 0.605$); however, E_{ZX} in adduction averaged 0.0113 ± 0.009 that was significantly greater than zero ($P < 0.0001$, Fig. 12). Strain E_{ZX} can be considered to represent nasotemporal tilting of the tissues by 1.3°.

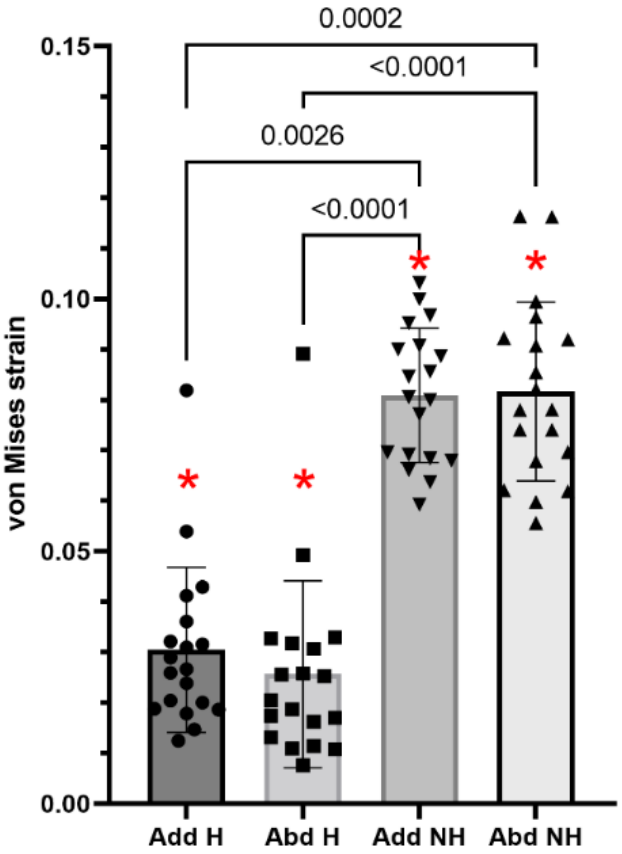

Figure 13. Gaze-evoked von Mises strains computed for homogeneous (H) and nonhomogeneous (NH) deformation. Add – adduction. Abd - abduction. Each symbol represents one of the 19 individual eyes. The Friedman test was used, and the asterisk represents data that is significantly different from zero. Error bars are standard deviations.

For homogeneous deformation analysis, all tissues are assumed similar, so that vessels and all other tissues behave similarly, on average. For nonhomogeneous analysis, deformations may differ in vessels versus other tissues. I compared average von Mises strains assuming homogeneous versus nonhomogeneous deformations (Fig. 13). For homogeneous deformation, adduction and abduction induced strains were similar at 0.030 ± 0.016 and 0.026 ± 0.018, respectively ($P > 0.999$). The strain level is consistent with the previous empirical data and finite element analysis for the optic disc[15, 62]. On the other hand, allowing for nonhomogeneous deformation, adduction and abduction caused greater strains of 0.081 ± 0.013 and 0.082 ± 0.017, respectively, that remained statistically similar to one another ($P > 0.999$). This indicates that the vasculature undergoes greater deformation that than other disc tissues during horizontal duction.

Also considering nonhomogeneous analysis, I also compared strains in the nasal versus temporal hemidiscs (Fig. 14). For adduction, normal strain E_{XX} in nasal hemidiscs was significantly greater than in temporal hemidiscs, although no other hemidisc differences was significant for adduction strains in other directions, nor for any direction in abduction. Absence of significant differences in these directions suggests that compression is acting to cancel tensile strain in temporal hemidisc when an eye is adducted, so the resultant strain is close to zero. Thus, I divided the strains into compressive and tensile strains. The compressive strain in temporal hemidisc was -0.033 ± 0.011, significantly larger than strain in the nasal hemidisc at -0.027 ± 0.013 (Fig. 15A). However, tensile strains did not differ significantly between hemidiscs (Fig. 15B).

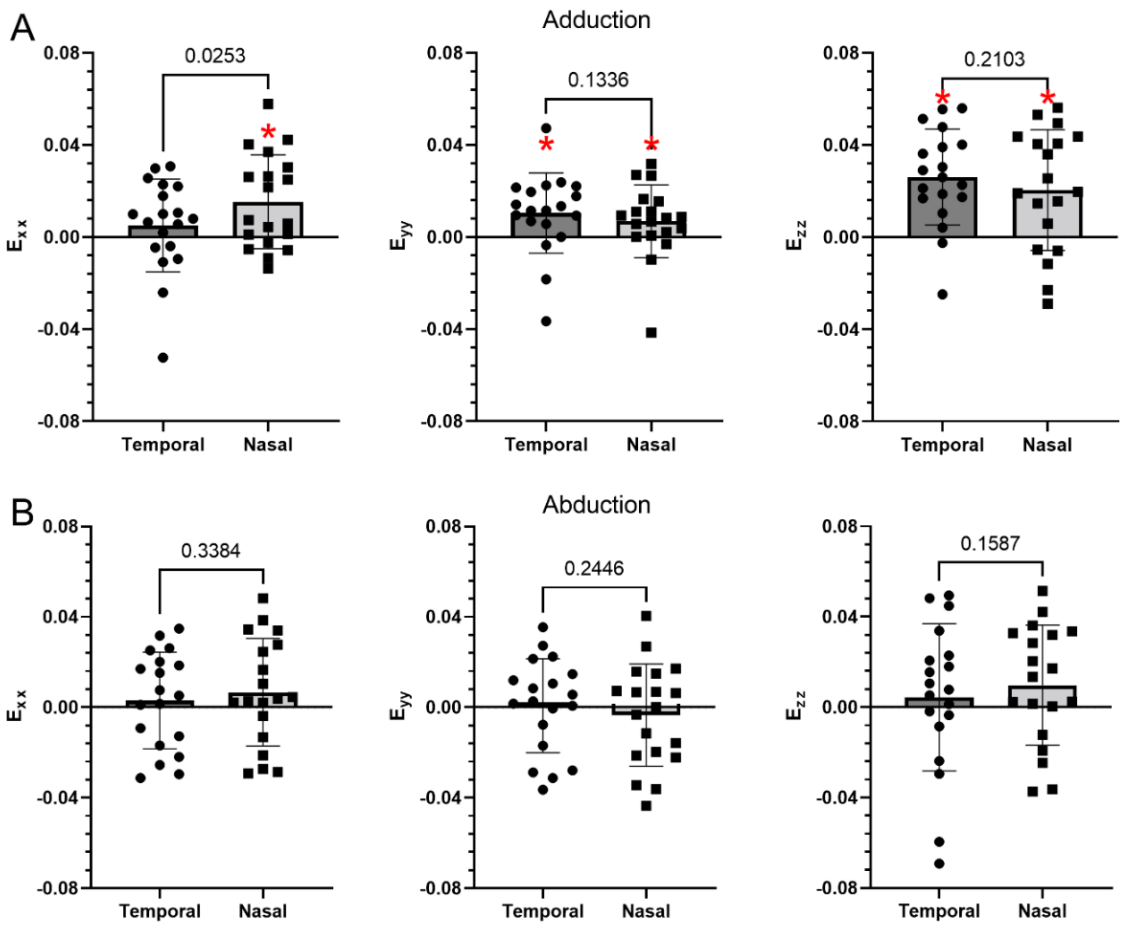

Figure 14. Normal strains in temporal and nasal hemidiscs for (A) adduction and (B) abduction. Each symbol represents one of the 19 individual eyes. The paired t-test was used, and asterisk represents data that is significantly different from zero ($P<0.005$ for each). Error bars are standard deviations.

In adduction, the x-directional (horizontal) normal strains in the temporal hemidiscs differed significantly from those in nasal regions. Bruch's membrane opening is a strong, elastic membrane that separates the retina from the underlying choroid, but has an opening at the optic disc through which ganglion cell axons pass to enter the optic nerve. the x-directional strain

difference his may be due to compression of vessels and other tissue within the Bruch's membrane opening, which as a region lacking Bruch's membrane support, offers less resistance to compression, and consequently concentrates stresses at its border. To ascertain if strain findings are related to Bruch's membrane opening compression, I computed the change in Bruch's membrane opening diameter caused by horizontal duction based on its cross sectional area, assuming circularity (Fig. 16). Bruch's membrane opening diameter after adduction was 0.989 ± 0.015 relative to its central gaze diameter, whereas the ratio was 1.004 ± 0.016 for abduction. Thus Bruch's membrane opening diameter is significantly decreased in adduction (P=0.009) but not in abduction (P=0.253).

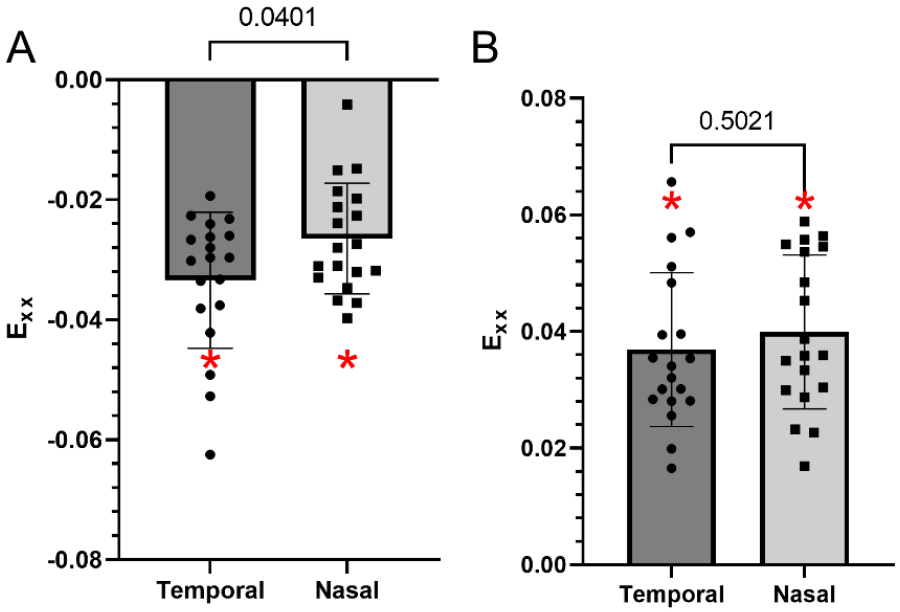

Figure 15. Compressive (A) and tensile (B) strains (E_{XX}) in temporal and nasal hemidiscs during adduction. Each symbol represents one of the 19 individual eyes. The Wilcoxon test and paired t-test were used for compressive and tensile strains, respectively. The asterisk represents data that is significantly different from zero (P<0.0001 for each). Error bars are standard deviations.

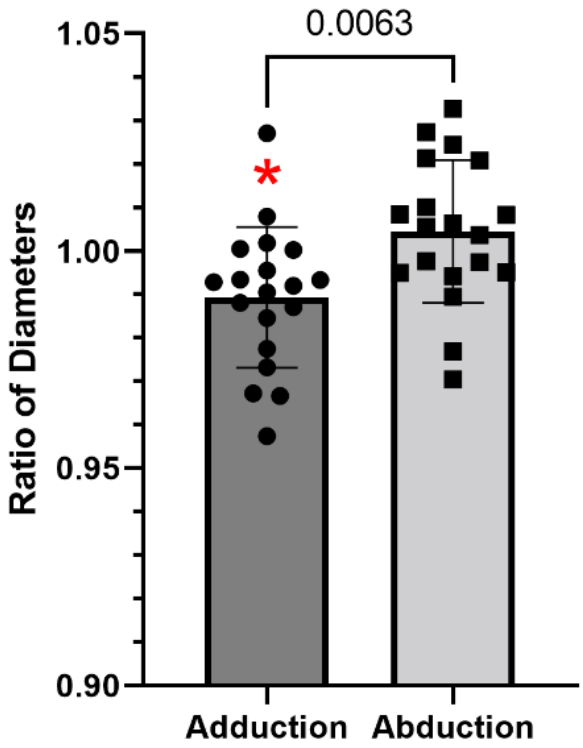

Figure 16. Change from central gaze in Bruch's membrane opening diameter due to horizontal duction in 19 eyes of 10 subjects represented by an individual. Asterisk represents data significantly different from unity by paired t-testing. Error bars are standard deviations.

From the results of this study, I conclude that traction force exists by measuring the increases of the blood vessels during horizontal duction. Since the driving force is now shown to work toward the posterior eye, the next questions were whether the source of the force is indeed the optic nerve.

CHAPTER 4. Validation and Quantification of Optic Nerve Strain Due to Horizontal Duction

Publications included in this chapter:

Lim S, Demer JL. Empirical Quantification of Optic Nerve Strain Due to Horizontal Duction. *Bioengineering* 2023;10;931.

To answer the question on whether the source of the driving force inducing mechanical deformation of the eye during adduction is the optic nerve, I employed magnetic resonance imaging because it offers a wide field of view and is not limited by optical transparency. Except for theoretical finite element analysis studies, however, local strains on the optic nerve have not been reported because of limitations of imaging modalities. The penetration depth of optical coherence tomography is a few hundred micrometers[63], which is not sufficient to reach the retrobulbar space. On the other hand, magnetic resonance imaging can visualize deep posterior regions of an eye, but its resolution is not as high as optical coherence tomography. Although the image resolution in theory may be improved as the magnetic field strength increases, the resolution of magnetic resonance imaging is about 200 μm even when the magnetic field strength is 7 T[64]. However, the static magnetic field of magnetic resonance imaging systems at the clinic are usually 1.5 T or 3 T, and physiological concerns regarding ultra-high field magnetic field exist[64]. Moreover, magnetic resonance imaging at high magnetic fields is susceptible to motion artifacts, compromising the image quality[65].

I considered the limited resolution of magnetic resonance imaging a bottleneck for the further research on eye movement, and hence parameterized a geometry of an optic nerve and developed a way of measuring strains of an optic nerve by eye rotation *in vivo*. By applying the method to ocular images from normal healthy people (mean ± standard deviations, 59 ± 16 years; 6 men and 6 women), I quantified the mechanical deformations of an optic nerve in a standardized process. As a result, I could prove and develop the theoretical framework to explain mechanisms for optic nerve traction and eye rotation.

The magnetic resonance imaging was conducted by using Signa 1.5 T scanner (GE Healthcare, Chicago, IL, USA) with ocular surface coils (Medical Advances, Milwaukee, WI, USA). The eye position was fixed at the central gaze or abduction, and the fellow eye was at adduction during the abduction fixation. Imaging was performed in axial planes and quasi-coronal planes. The resolution of axial plane and quasicoronal images were 390 μm and 312 μm, respectively.

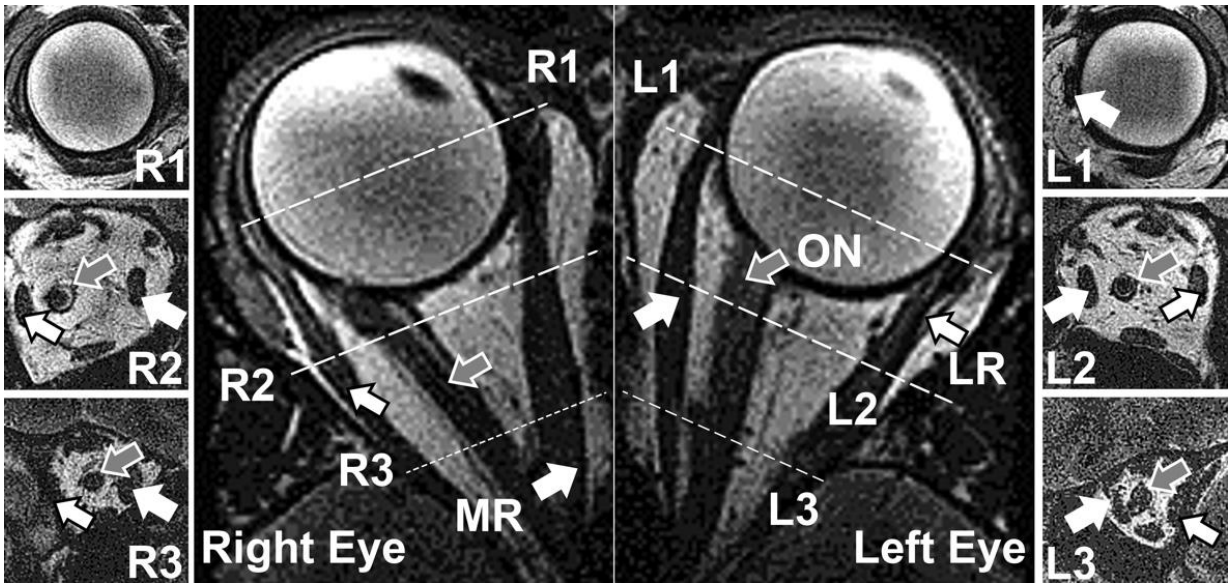

Figure 17. Representative quasicoronal (resolution 312 μm) and axial (resolution 390 μm) magnetic resonance imaging for a subject in large angle left gaze. R1, R2, and R3 images represent anterior, medial, and posterior section of the right orbit, obtained in the planes indicated by the dotted lines. Similarly, L1, L2, and L3 correspond to anterior, medial, and posterior section of the left orbit. MR – medial rectus muscle. LR – lateral rectus muscle. ON – optic nerve. White arrows indicate medial rectus muscles, and arrows with black edges represent lateral rectus muscles. Gray arrows point to optic nerves.

I manually identified the globe, optic nerve, orbital wall, lateral rectus, and medial rectus muscles in coronal and axial magnetic resonance images. Then video frame interpolation was performed along the axis, which is perpendicular to the image plane[66]. The segmented pixels from each image stack were converted to 3D point-sets. Rigid point-set registration[67] was performed between coronal and axial images. Because the coronal image set did not completely span the anterior globe, I used point clouds that correspond to the completely-imaged optic nerve, lateral

and medial rectus muscles for this registration. Point-sets from lateral and medial rectus muscles were used to prevent ambiguity due to axisymmetric optic nerve geometry. Finally, I registered point clouds between primary gaze and horizontal duction assuming that points for the bony orbital wall are not displaced by eye rotation.

After finishing the point-set registration, I could combine the point clouds from axial and coronal magnetic resonance imaging. Then I identified centroids of the optic nerve along its length. Because a convex hull could be defined from the points for the globe, the intersection point between the convex hull and a line through the most anterior two optic nerve centroids was regarded as the optic nerve junction, and the normal vector for the hyperplane that includes the optic nerve junction defined the gradient of the optic nerve trajectory at the optic nerve junction. Because the orbital apex was not visible in magnetic resonance imaging data, I also estimated its location. An adducted eye has a stretched optic nerve; therefore, its linear line would be directed to the orbital apex. By extrapolating the orbital wall, I identified the point where the stretched optic nerve meets the orbital wall, and considered this point as this orbital apex. The optic nerve centers, the optic nerve junction, and the orbital apex became knot points for the parameterization, and a curve to pass through the points was defined by parametric curve fitting[68].

Because I could register axial with coronal magnetic resonance imaging, by reciprocity, coronal could also be registered to axial magnetic resonance imaging. By the registration from coronal images for the left and right eyes to axial images, the orbital walls were registered bilaterally. Then I found the medial plane to minimize the Chamfer distance between the reflected point-set from one eye and its fellow by using optimization. Chamfer distance is a metric to compute the similarity between two different point clouds[69], so I could estimate the best-fitted medial plane whose normal vector serves as the X-axis. Also, I identified the junction of the

superior ethmoid air sinus and orbit as the anterior ethmoid recess[70]. Then I rotated the line connecting the junctions by 10° in the medial plane, and the rotated line defined the Z-axis. The Y-axis was determined by the cross-product between the X- and Z-axes. By using the standardized coordinate system based on eye socket structure, I could compare data among different globes.

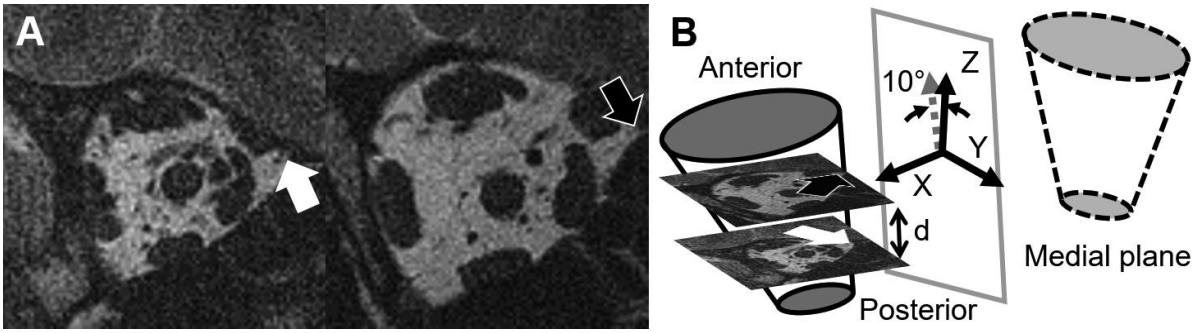

Figure 18. Definition of the coordinate system. (A) Quasicoronal MRI from a right eye. The arrows represent the anterior ethmoid recess in two different image planes. (B) By reflecting the orbital wall point-set, a medial plane is defined, and its normal defines the X-axis. Because coordinates of the anterior ethmoid recess and the distance between image planes are known, the pitch angle of the orbit can be calculated. The gray dashed arrow represents the vector between 3D coordinates of the anterior ethmoid recess in separate quasicoronal image planes, and the vector's direction is used to define Z-axis after rotating 10° in the medial plane. The Y-axis is orthogonal to the X- and Z-axes, and is positive to-wards the top of the head.

Because the optic nerve path was parameterized, its tangent vector could be determined. Then a plane whose normal vector is a tangent vector of the optic nerve path and the origin is a point in the curve could be determined. By the projection of the adjacent optic nerve points on the plane, optic nerve cross-section in each plane was determined. For the projected points, I could

obtain the convex hull for the points. Because the convex hull set the boundary of the cross-section, I could parameterize the local polar coordinates on the plane. The volume of optic nerve was measured by a summation of the products of a cross sectional area and a length of line segment in the optic nerve path.

To compute displacements for points in the initial configuration, corresponding points on the deformed configuration were identified by the parameterization. By subtracting the coordinates between initial and deformed configurations, I could obtain displacements. Then gradients of the displacements were necessary for computing strains. However, because point clouds are unstructured data, the gradients along the X-, Y-, and Z-axes could not be obtained straightforwardly. Instead, I found 6 nearest neighbors for each point and computed the directional derivatives along each vector. Because the X-, Y-, and Z-axes could be represented by a linear combination of 6 vectors, I obtained the gradient of the displacements by the linear combination of the directional derivatives. For a unit vector that is parallel to each axis, the unit vector can be represented by a linear combination of 6 unparalleled vectors $\underline{e} = k_1\underline{v_1} + k_2\underline{v_2} + k_3\underline{v_3} + k_4\underline{v_4} + k_5\underline{v_5} + k_6\underline{v_6}$. The equation can be rewritten in a matrix form as follows. $\underline{e}$=VK where $\underline{e}$ is a unit vector for each axis, V is the matrix whose column vectors are normalized vectors between each point and 6 nearest points, and K is a matrix whose elements are undetermined coefficients for the linear combination, respectively. Then $V^T\underline{e}=V^TVK$ where V^T is the transpose of matrix V. As a result, the coefficients could be determined by using the pseudo inverse matrix. $K=(V^TV)^+V^T\underline{e}$ where $(V^TV)^+$ is the pseudo inverse matrix of V^TV.

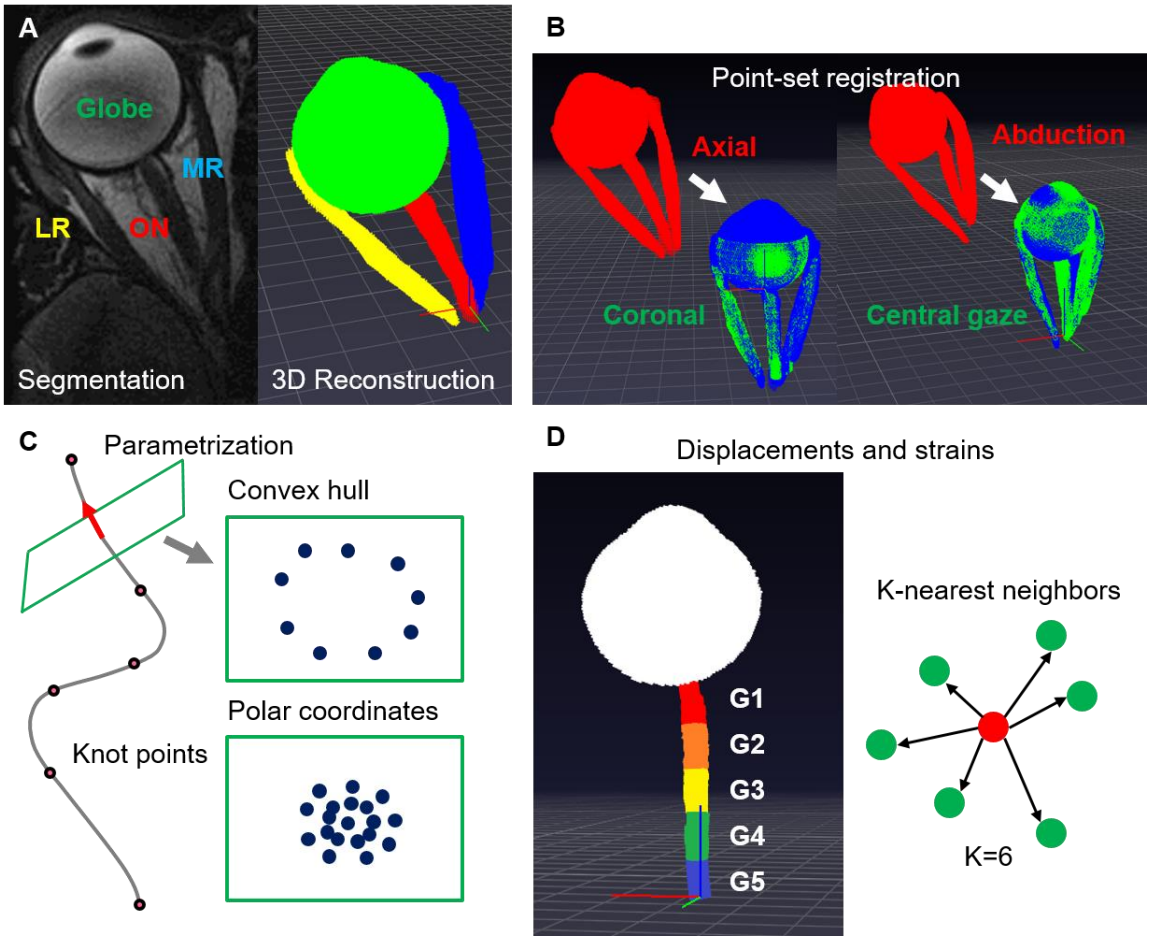

Figure 19. Workflow to measure displacements and strains after eye rotation. (A) Globe, optic nerve, and extraocular muscles are segmented from magnetic resonance imaging data, and the pixels in the image stack are converted to 3D point-sets. (B) Point-set registration between axial and coronal view images, and between images obtained in different eye positions. (C) Centroids of optic nerve segments works as knot points for a curve to parameterize the optic nerve path, and a local polar coordinate system on the plane tangent to the curve parameterizes optic nerve cross section. (D) Displacements of the optic nerve are computed by comparing deformed and initial configurations, and the data is grouped into 5 segments depending on location along optic nerve length. The gradients of displacements are calculated by comparing 6 nearest neighbor points, and the gradients determine strains.

I measured the geometry related to horizontal duction. The angles of rotation and torsion for an eye were measured, depending on the eye position. From the point-set representing the surface of the eyeball, I identified the cornea apex and a point that is farthest from the apex. The farthest point on the surface is the fovea, and the visual axis was defined to be a line spanning from the cornea apex to the fovea. The angle between the visual axis and the Z-axis for the globe was considered an angle of rotation. Moreover, I identified lateral and medial rectus muscle insertions for a globe and measured the angle of torsion to register the insertions between globes under different eye positions. Abduction angles for primary gaze, large adduction, large abduction, moderate adduction, and moderate abduction were 9.8 ± 1.1° (mean ± standard error), -28.1 ± 1.0°, 30.4 ± 1.3°, -23.8 ± 0.9°, and 24.2 ± 1.0°, respectively.

Tortuosity is defined to be the ratio of actual optic nerve path length to the straight line (minimal) distance between the optic nerve junction and orbital apex. Tortuosity for primary gaze, large adduction, large abduction, moderate adduction, and moderate abduction were 1.023 ± 0.004 (mean ± standard error), 1.017 ± 0.002, 1.036 ± 0.004, 1.016 ± 0.002, and 1.029 ± 0.003, respectively. These results indicate that adduction straightens the optic nerve path, while abduction does not. Also, the torsion angle changes for the large adduction, large abduction, moderate adduction, and moderate abduction were 0.62 ± 0.58° (mean ± standard error), 0.08 ± 0.62°, 1.55 ± 0.57°, and 0.33 ± 0.44°, respectively. Because the measured torsion angle changes were much smaller than the magnitudes of duction angle, I considered bending motion to be dominant compared to the twisting of the optic nerve during duction.

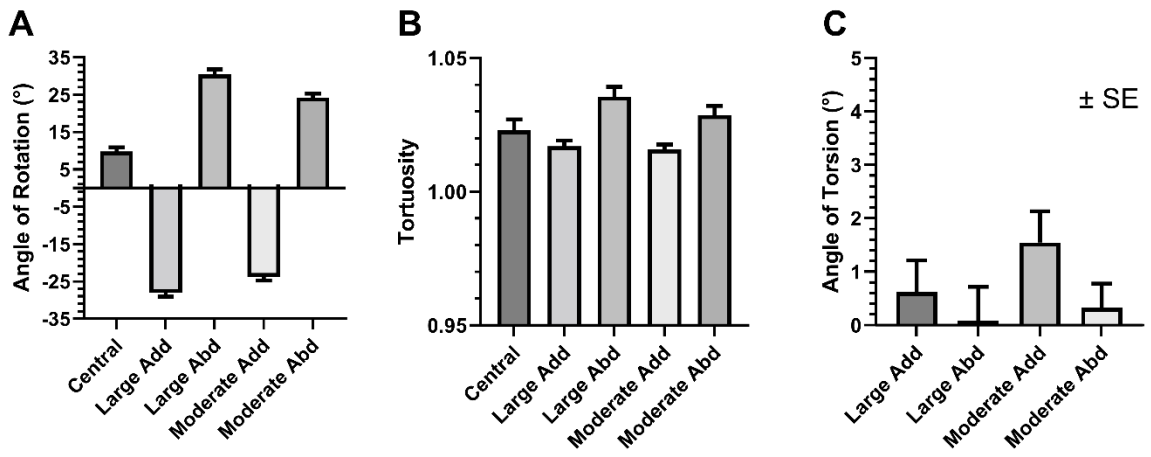

Figure 20. Changes due to horizontal duction. (A) Eye orientation relative to the medial plane of the head. (B) Tortuosity, the ratio of actual optic nerve length to length of straight line from the optic nerve junction to the orbital apex. (C) Ocular torsion did not change significantly with duction. SE – standard error of the mean. Abd – abduction. Add – adduction.

The point on the globe farthest from the cornea was taken to approximate the fovea; this approximation neglects the visual angle kappa, but results in a consistent representation that accurately captures changes in eye orientation. Then I defined the optic nerve junction with the globe as the origin of a local coordinate system, with the X-axis defined by the line between the fovea and optic nerve junction. The Z-axis (posterior-anterior) was parallel to the normal vector of the globe surface at the optic nerve junction, and the Y-axis was orthogonal to the X- and Z-axes. This enabled standardization of data using a coordinate system based on biological landmarks. In addition, I defined a local coordinate system at each center point of the cross section along an optic nerve path. The local Z-axis is parallel to the tangent vector of the parameterized curve, and the local X-axis is the projection on the plane whose normal vector is the local Z-axis.

The local Y-axis is also perpendicular to both the local X- and Z-axes. Based on the local coordinates system and the parameter for the curves, I could identify corresponding matched points for the optic nerve between gaze directions.

By using the method above, I measured the translation of the center point for each globe after duction. Data are plotted for horizontal translation in Fig. 21A. For large adduction, the globe translated medially by 1.08 ± 0.24 mm. For large abduction, the globe laterally translated 0.80 ± 0.22 mm. For moderate adduction the globe translated nasally by 0.65 ± 0.18 mm. For moderate abduction, the globe translated temporally by 0.78 ± 0.21 mm. Corresponding small superior (Y axis) translations were -0.05 ± 0.20 mm, 0.04 ± 0.26 mm, 0.01 ± 0.22 mm, and 0.00 ± 0.18 mm, respectively; none of these differed significantly from zero (Fig. 21B).

The globe translated posteriorly for both directions of horizontal duction (Fig. 21C). The magnitudes of the displacement from large adduction, large abduction, moderate adduction, and moderate abduction were -0.111 ± 0.191 mm, -1.185 ± 0.166 mm, -0.131 ± 0.186 mm, and -0.711 ± 0.147 mm, respectively. The magnitude of the anteroposterior translation is larger in abduction than in adduction ($P<0.0001$).

In addition, I measured the magnitude of combined 3D globe translation during ductions (Fig. 21D). The 3D magnitudes for large adduction, large abduction, moderate adduction, and moderate abduction were 1.98 ± 0.13 mm, 2.10 ± 0.20 mm, 1.62 ± 0.14 mm, 1.65 ± 0.17 mm, respectively.

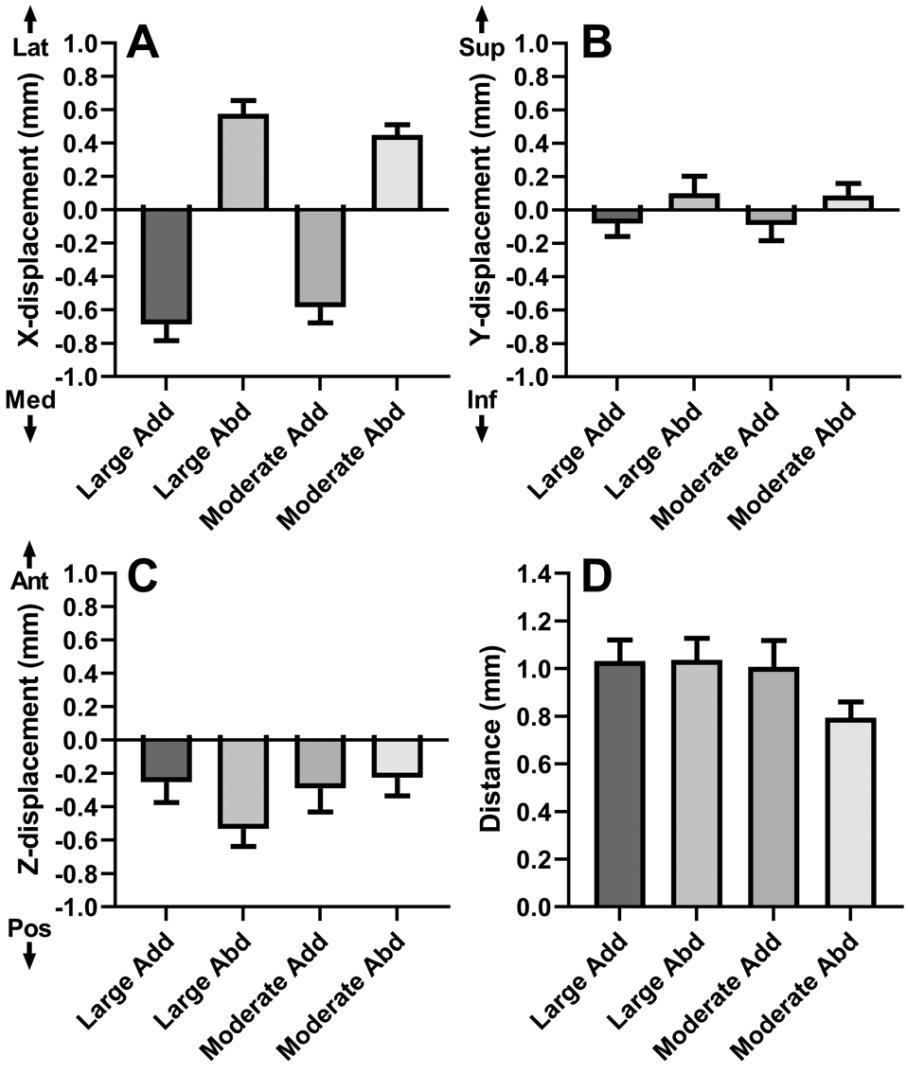

Figure 21. Globe translation after horizontal duction. (A) Mediolateral. (B) Vertical (C) Anteroposterior. (D) Magnitude of 3D translation. Abd – abduction. Add – adduction. SE – standard error of the mean.

I measured local 3D displacements of the optic nerve due to duction in five regions of equal length along its anteroposterior extent. Region G1 is closest to the globe- optic nerve junction, and G5 is closest to the orbital apex. As seen in Fig., 22, displacements were greatest anteriorly and

progressively decreased in posterior regions; this effect was significant for large and moderate ab- and adduction ($P < 0.001$, ANOVA).

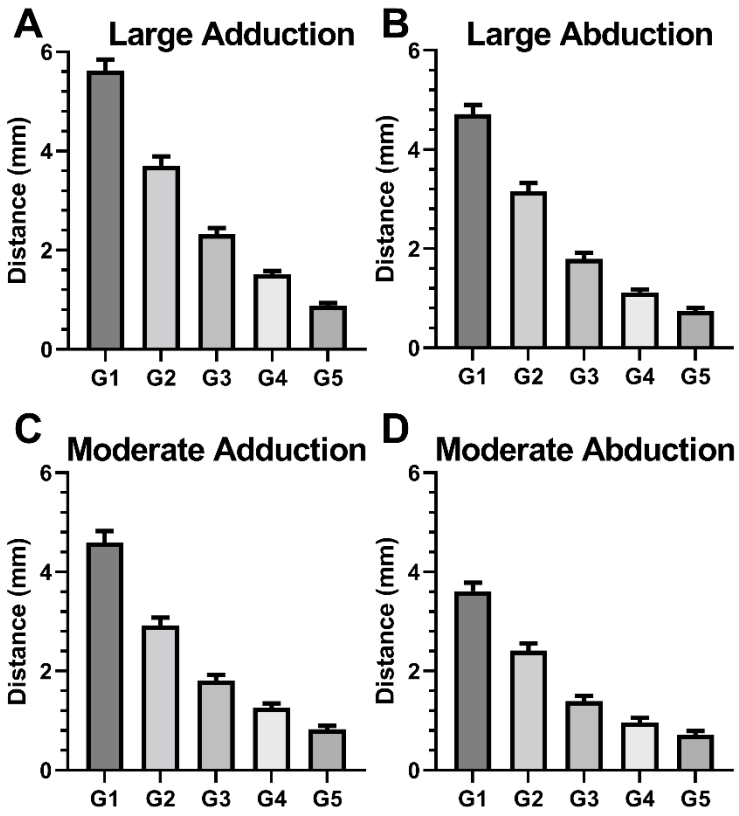

Figure 22. Regional 3D displacements of the optic nerve for (A) large adduction, (B) large abduction, (C) moderate adduction, and (D) moderate abduction. G1 through G5 are equal intervals along the optic nerve length from anterior to posterior, respectively. SE – standard error of the mean.

I computed the optic nerve strains by differentiating local optic nerve displacements for the direction tangent to optic nerve path in the optic nerve regions into 5 regions as defined above (Fig. 23). Local strain behavior differed fundamentally between ad- and abduction. Strains were about

5% for large and 4% for moderate adduction, but did not vary significantly by region for either ($P>0.5$ for each, Friedman test), whereas strains varied depending on locations for large and moderate abduction ($P<0.05$ for each). In contrast, for both moderate and large abduction, strain was least at about 1% in region G1 that abutted the globe, and increased monotonically to about 4% in region G5 at the orbital apex. For abduction, strain did not depend significantly on duction size, but did depend on region. As a result, the strains in G1, G2, G3, G4, and G5 were 0.055 ± 0.017, 0.054 ± 0.011, 0.058 ± 0.011, 0.049 ± 0.009, and 0.057 ± 0.014 in large adduction, while large abduction led to strains of 0.011 ± 0.013, 0.010 ± 0.013, 0.020 ± 0.013, 0.032 ± 0.011, and 0.037 ± 0.010 in each region. Moderate adduction resulted in the optic nerve strain of 0.051 ± 0.018, 0.043 ± 0.010, 0.037 ± 0.007, 0.042 ± 0.007, and 0.048 ± 0.012 in each region. In the case of moderate abduction, the strain values were 0.014 ± 0.011, 0.007 ± 0.014, 0.021 ± 0.016, 0.033 ± 0.011, and 0.046 ± 0.011 in each region.

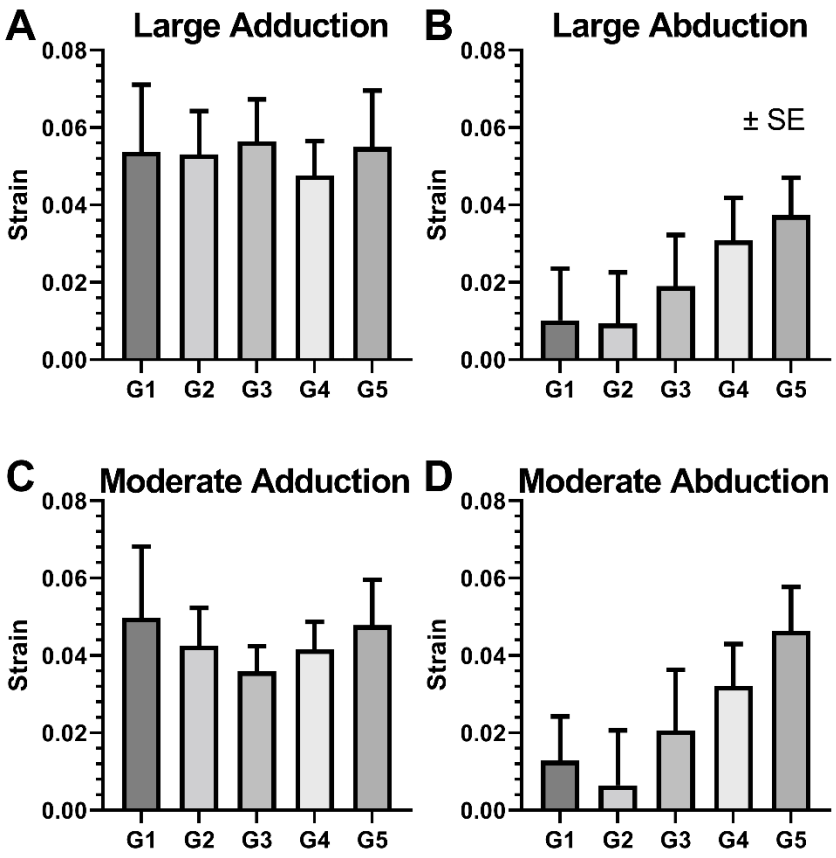

Figure 23. Local strains E_{zz} along the path of the optic nerve depending on the region for (A) large adduction, (B) large abduction, (C) moderate adduction, and (D) moderate abduction. Strain did not vary significantly along the length of the optic nerve in adduction, but increased progressively towards the orbital apex for both large and moderate abduction. G1 through G5 are equal intervals along the ON length from anterior to posterior, respectively. SE – standard error of the mean.

The ratios of inner and outer diameters of the optic nerve sheath to optic nerve diameter were invariant after adduction (Fig. 24; P>0.688 for each, generalized estimating equation). The ratio for the inner diameter was approximately 1.5, whereas the ratio for the outer diameter was approximately 1.9. Assuming the volume conservation of the optic nerve and its sheath during

uniform stretching, $L_{central}A_{central,ONS} = L_{add}A_{add,ONS}$ and $L_{central}A_{central,ON} = L_{add}A_{add,ON}$ are derived where L_{α} and $A_{\alpha,\beta}$ are length and cross-sectional area of tissue β in the eye position α. Thus, $\frac{L_{add}}{L_{central}} = \frac{A_{central,ONS}}{A_{add,ONS}} = \frac{A_{central,ON}}{A_{add,ON}}$. The second equality implies $\frac{d_{central,ONS}}{d_{add,ONS}} = \frac{d_{central,ON}}{d_{add,ON}}$, followed by $\frac{d_{central,ONS}}{d_{central,ON}} = \frac{d_{add,ONS}}{d_{add,ON}}$ where $d_{\alpha,\beta}$ is the diameter of the cross-section of tissue β in the eye position α. This analysis can be valid for both inner and outer diameters. Therefore, the data in Fig. 24 suggest that the optic nerve and its sheath stretch by similar amounts during adduction tethering, supporting the optic nerve traction hypothesis.

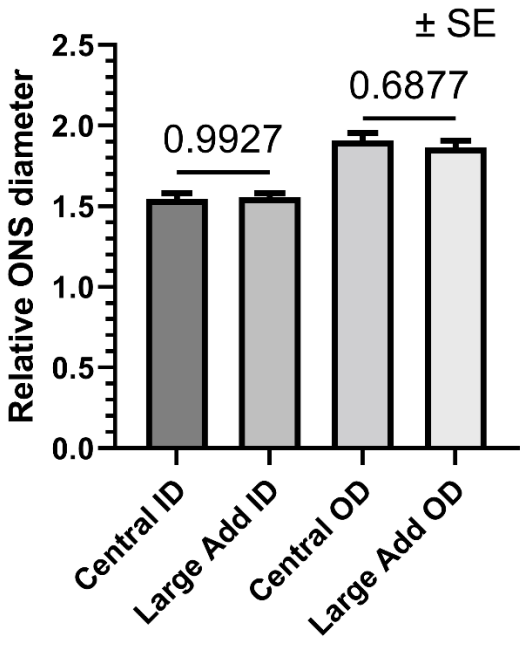

Figure 24. Ratios of optic nerve sheath diameters to the optic nerve diameter before and after adduction. ID and OD stand for inner and outer diameters. Add – adduction. The error bar represents the standard error of the mean. The method of generalized estimating equations was used for statistical analysis.

Through this research, the analysis of magnetic resonance imaging demonstrates that the optic nerve behaves like a stretched truss in adduction, whereas the optic nerve deforms like a cantilever beam in abduction. As a result, I could confirm that the traction force during horizontal duction is generated by the optic nerve and its sheath. By sequential studies from **Chapter 2** to this current chapter, a fundamental part of the optic nerve traction hypothesis itself has been validated. My next question is whether the traction force can be significantly transferred to the eyeball, and this question is addressed in the following **Chapter 5**.

CHAPTER 5. 3D Digital Image Correlation Illustrates that Traction Force from Adduction is Transmitted to the Eyeball.

The manuscript included in this chapter:

Lim S, Kim C, Jafari S, Park J, Garcia SS, Demer JL. Postmortem Digital Image Correlation and Finite Element Modeling Demonstrate Posterior Scleral Deformations During Adduction Tethering. submitted, 2023.

Looking back the history of the optic nerve tethering hypothesis, magnetic resonance imaging showed that large angle ocular adduction stretches the optic nerve and its sheath[10]. From the observation, the stretched optic nerve and its sheath were supposed to induce traction force on the optic disc and peripapillary region[10]. Although the connection between eye movement and the optic disc had not been appraised, this speculation encouraged studies on deformations of posterior regions due to eye movement. Sibony published a report on deformations of peripapillary basement membrane layer by horizontal duction[71]. Further optical coherence tomography studies quantified strains, relative displacements, tilting, and local area changes of the optic nerve head associated with horizontal eye rotation[51, 62, 72, 73]. In addition to anteroposterior deformations from horizontal eye rotation, deformations within the plane of the retina were also measured by computing displacements and strains of retinal blood vessels[14, 74, 75]. As further research has progressed, the optic nerve tethering theory has been developed. Biomechanical simulations of optic nerve traction have been presented[16, 76, 77], and active contraction of extraocular muscles has

been included to the simulation model for the realistic prediction[35]. Diverse experimental approaches which used scanning laser ophthalmology[14, 74], optical coherence tomography[13, 62, 75, 78], and magnetic resonance imaging[18, 79, 80] also supported the optic nerve traction theory.

Even before my dissertation, the adducted optic nerve had been clearly visualized to become straight and apparently taut by magnetic resonance imaging[10]. Significant deformations of the optic disc and peripapillary regions due to eye rotation were also observed in previous studies[13, 62, 72, 73]. However, because stresses and strains from adduction are highly dependent on relative magnitudes of stiffness for different ocular regions[77], the linkage between the taut optic nerve and deformations in the eyeball is not necessarily clear. For example, if the optic nerve and its sheath were more compliant than sclera, the taut optic nerve may not transmit sufficient force to induce significant deformations in the eyeball. The optic nerve sheath Is known to exhibit low elastic modulus[81].

The previous optical coherence tomography analysis demonstrated that deformations from eye rotation become large when the angle of rotation exceeds 26°, and the angle has been considered the threshold angle to straighten the optic nerve path[13]. However, the driving force from incremental adduction beginning at 26° may not be sufficiently large to deform the eyeball and optic disc. To clarify this uncertainty and strengthen the optic nerve tethering theory, I incorporated the concept of strain stiffening[82] into the optic nerve tethering theory. Elastic moduli of biopolymers often increase with increasing strain, and this nonlinear behavior is called strain stiffening[82]. Collagen exhibits strain stiffening[83], and is a primary component of the optic nerve sheath[84], so the optic nerve sheath exhibits nonlinear strain stiffening.

Although relationships between the optic nerve tethering and etiology requires further studies, I attempted to validate optic nerve traction itself clearly throughout this study. Since the

in vivo imaging of posterior sclera at high resolution is impossible at high resolution[85], I designed an *ex vivo* experiment to validate that adduction can induce deformations of human ocular tissues. The ocular surface was analyzed by a 3D digital image correlation algorithm[47]. Moreover, I analyzed effects of strain stiffening on mechanical deformations in adduction by using finite element analysis. Through experimental and numerical approaches, this study examined if the driven force from the optic nerve tethering is large enough to deform the eyeball.

Methods

Overall workflow (Fig. 25). Human eyes with attached optic nerves averaging 17.9 ± 2.9 (standard deviation, SD) mm long were shipped to the laboratory by the Lions Gift of Sight Eye Bank (Saint Paul, MN, USA) shortly after donors' death. Each specimen was tested using 3D digital image correlation under loading by adduction tethering from 26 – 32°, as well as by intraocular pressure elevation. The globes and optic nerves were then divided into specimens that were subjected to tensile testing. Stress-strain curves obtained by tensile testing were employed as inputs to finite element models individualized to each eye whose behavior under intraocular pressure elevation and adduction tethering was compared with 3D digital image correlation.

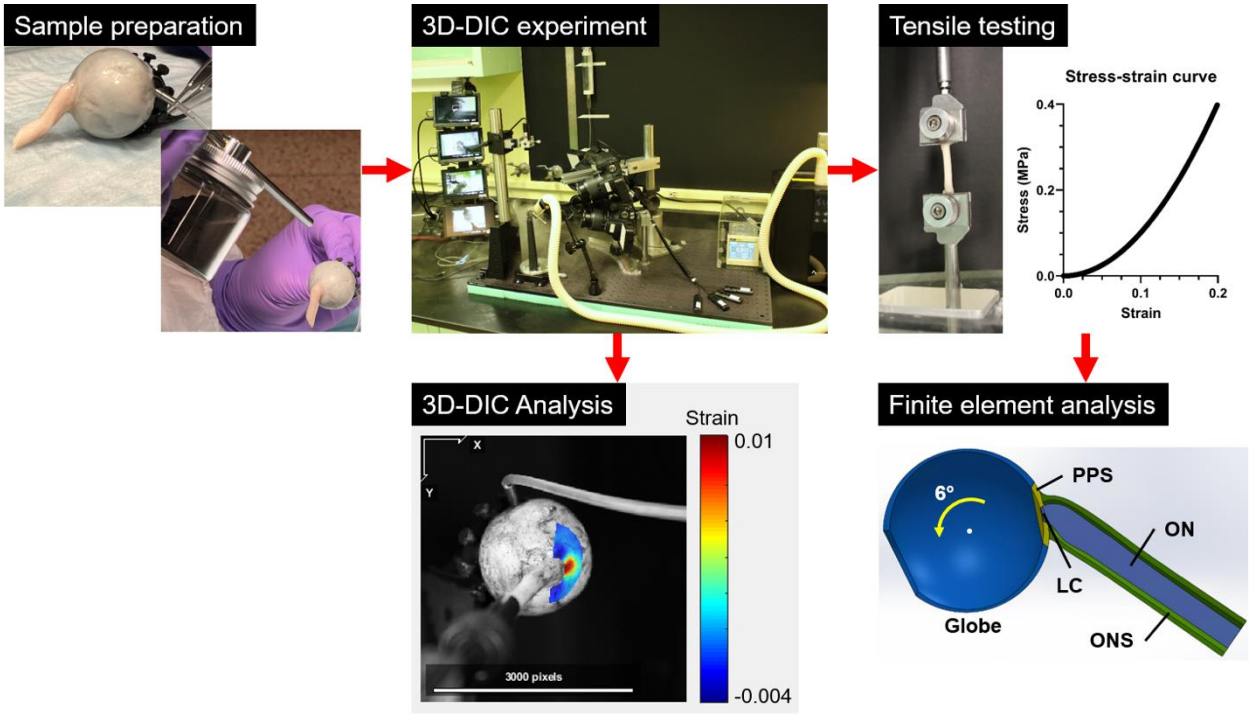

Figure 25. Investigation workflow. After preparing the specimen, a 3D digital image correlation experiment was performed to quantify the effect of adduction tethering and intraocular pressure elevation. Then, uniaxial tensile testing was conducted to characterize material properties of each specimen that were used for finite element analysis numerical simulation, and comparison with 3D digital image correlation analysis. The heat map for digital image correlation analysis shows horizontal strains. PPS - peripapaillary sclera. LC - lamina cribrosa. ON - optic nerve. ONS - optic nerve sheath.

Specimen preparation. Specimen donors had consented to use of their eyes for research. Specimens wrapped in cotton gauze moistened with saline in insulated containers cooled with ice packs were air shipped to the laboratory an average 39 ± 12 hours following enucleation. Donors were white, with average age 74.1 ± 9.3 years. There were five males and two females.

Table 1. Specimens tested

No.	Axial length (mm)	Transverse diameter (mm)	Optic nerve length (mm)	Optic nerve sheath radius (mm)	Time from enucleation to delivery (hours)
1	23.72	23.22	14.39	3.65	38
2	25.86	24.3	21.95	3.12	28
3	25.69	24.48	17.17	2.85	28
4	24.22	23.86	15.07	3.05	65
5	24.54	24.19	13.45	3.12	65
6	24.5	23.08	19.91	3.25	31
7	24.54	22.96	18.06	2.81	31
8	24.96	25.64	23.48	3.21	38
9	25.43	24.38	20.29	2.99	42
10	25.14	24.66	16.01	3.03	42
11	25.89	25.86	17.44	2.86	32
12	25.77	25.82	17.74	3.51	32

After removal of any overlying tissues, 6-0 coated Vicryl suture (Ethicon, Raritan, NJ, USA) was used to attach the anterior sclera onto multiple suturing posts on a custom aluminum fixation ring, passing partial thickness through the perilimbal sclera without perforation. The 45° internally beveled ring had 20 mm outer diameter and 16.5 mm inner diameter. Right eyes were sutured into the fixation ring with the superior region upward, whereas for left eyes, the orientation was downward. A stab incision was then made in the anterior sclera over the pars plana 3.5 mm from the limbus using a 23-gauge ophthalmic micro-vitreoretinal blade (Alcon, Geneva, Switzerland), through which a 23-gauge cannula (Bausch + Lomb, Laval, Canada) was inserted to maintain intraocular pressure by Ringer's lactate fluid infusion (Fig. 26A). Then, cast iron dust of mesh 150 (Chemical Store Inc., Clifton, NJ) was randomly scattered on the surface of the eyeball by using a pneumatic applicator (Elaimei, Portsmouth, UK) (Fig. 26B) to create a pattern suitable for imaging to compute deformations by 3D digital image correlation (Fig. 26C).

Figure 26. Sample preparation. (A) Globe was sutured to fixation ring, and infusion cannula inserted in anterior sclera. (B) Speckles of cast iron dust were randomly applied to the surface by using a pneumatic applicator. (C) Speckle pattern on the sclera.

Apparatus for 3D digital image correlation. The infusion cannula was connected to a fluid column containing Ringer's lactate solution (B. Braun Medical Inc., Bethlehem, PA, USA) via an infusion set (MedSource, Rancho Santa Margarita, CA, USA), allowing control of intraocular pressure by changing the height of the infusion fluid column relative to the center of the eye. The reference level of hydrostatic pressure was at 15 mmHg, and it could increase to 30 mmHg. During the experiments, warm mist at 30°C from an ultrasonic humidifier (Asakuki, Rochester, NY, USA) was directed to the specimen to suppress tissue dehydration.

A laser cross alignment projector (OXLasers Co., Ltd., Shanghai, China) was mounted above the system to align eye ocular center with the rotational center of a 300 mm radius curved translational bearing (Misumi, Tokyo, Japan). The distal end of the optic nerve was coaxially clamped by a custom gripper on a rod in mechanical series with a sensitive force sensor (FUTEK Advanced Sensor Technology, Irvine, CA, USA) that traveled along the bearing arc. Position of the terminal end of the rod was adjustable by vernier. The globe was positioned until its center

corresponded to the projected laser crosshair center. Then, the initial rotational position of the eye was set by a precision rotation mount (Thorlabs, Newton, NJ, USA). Initial optic nerve tension was set by extending the position of its terminal support rod until the force sensor demonstrated detectable tension. The length of the straight optic nerve and the transverse diameter of the globe were used for determining the initial and deformed configurations of the optic nerve during experiments, as described below.

Five Canon EOS Rebel T7 digital single-lens reflex cameras with 6000 by 4000 pixel resolution (Canon, Tokyo, Japan) were used to take images from multiple locations by using manual focus. Each camera was fitted with an EF-S 18-55 mm lens (Canon, Tokyo, Japan), with focal length set to 55 mm at which pincushion distortion was 0.2%. Remote controllers RS60 E3 (Canon, Tokyo, Japan) were used to avoid camera vibration. Although the conventional digital image correlation analysis may use as few as two cameras[86], five cameras were employed because of occlusions of some regions in some cameras due to the long optic nerve and its clamp. Thus, pairs of cameras could each image the nasal, superior, and temporal regions of sclera relative to the optic nerve attachment.

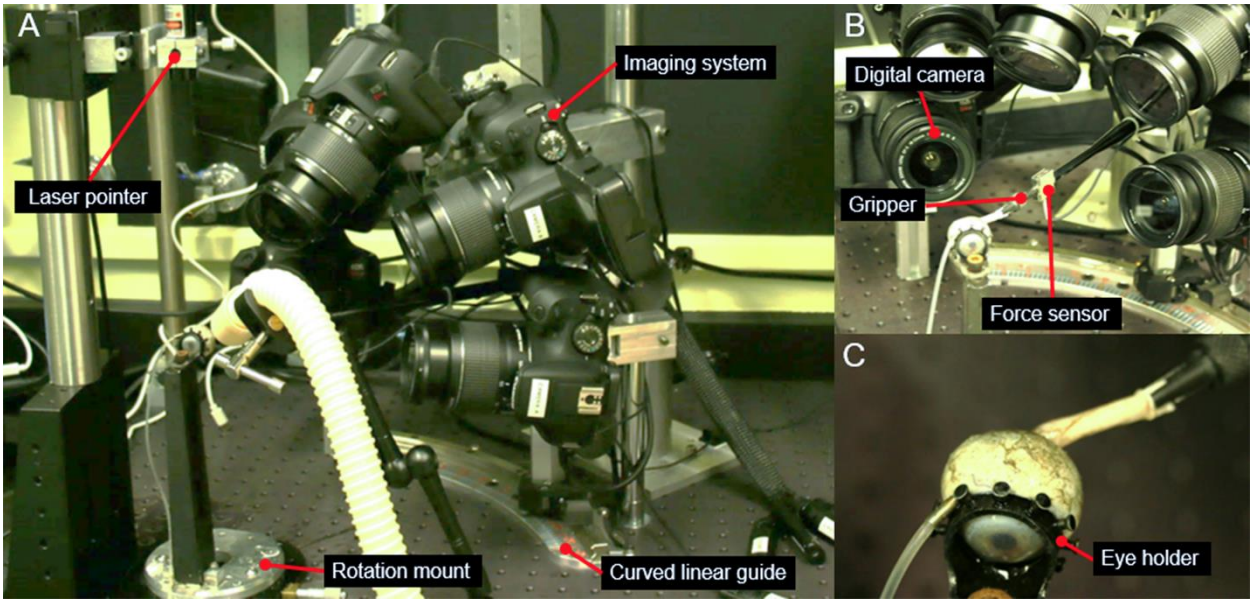

Figure 27. 3D digital image correlation setup. (A) overall system, including the eye warmed and humidified via the white humidified tube, cameras, and curve guide for the gripper holding the distal optic nerve. (B) close-up of imaging system. (C) magnified image the eye in its holder.

Geometric consideration for the digital image correlation setup. Because the centroid of the eye and the center of rotation of the curved translational bearing coincided, the coordinates of the optic nerve junction with the globe, and coordinates of the terminal optic nerve gripper can be represented by polar coordinates. Although physiologically the eye rotates in the head, in this 3D digital image correlation experiment, rotation of the eye relative to the camera array could have introduced imaging distortions that might have compromised accuracy of the results. A kinematically identical approach was taken that maintained a fixed location of the ocular center, but altered the relative rotational location of the optic nerve support that constituted the virtual orbital apex. According to nomenclature in Fig. 28, in the initial configuration of 26° adduction, the coordinates at the optic nerve junction are $(r\cos\phi, -r\sin\phi)$ where r and ϕ represent the globe radius and the azimuth of the optic nerve junction. At the same time, the coordinates at the

gripper are $(R\cos(\phi+\chi), -R\sin(\phi+\chi))$ where, R and χ represent the distance from the globe center to the gripper and the incremental angle to locate the gripper. In either rotating the eyeball or the gripper, the length of optic nerve at in additional adduction to 32° can be computed. In the initial configuration, optic nerve length becomes $(r^2 + R^2 - 2rR\cos(\chi))^{1/2}$. When the gripper is rotated by ψ, optic nerve length is $(r^2 + R^2 - 2rR\cos(\chi+\psi))^{1/2}$. Thus, $\theta = \psi$ implies that the optic nerve lengths at the two cases are equal, indicating that rotating the gripper is kinematically equivalent to rotating the eye.

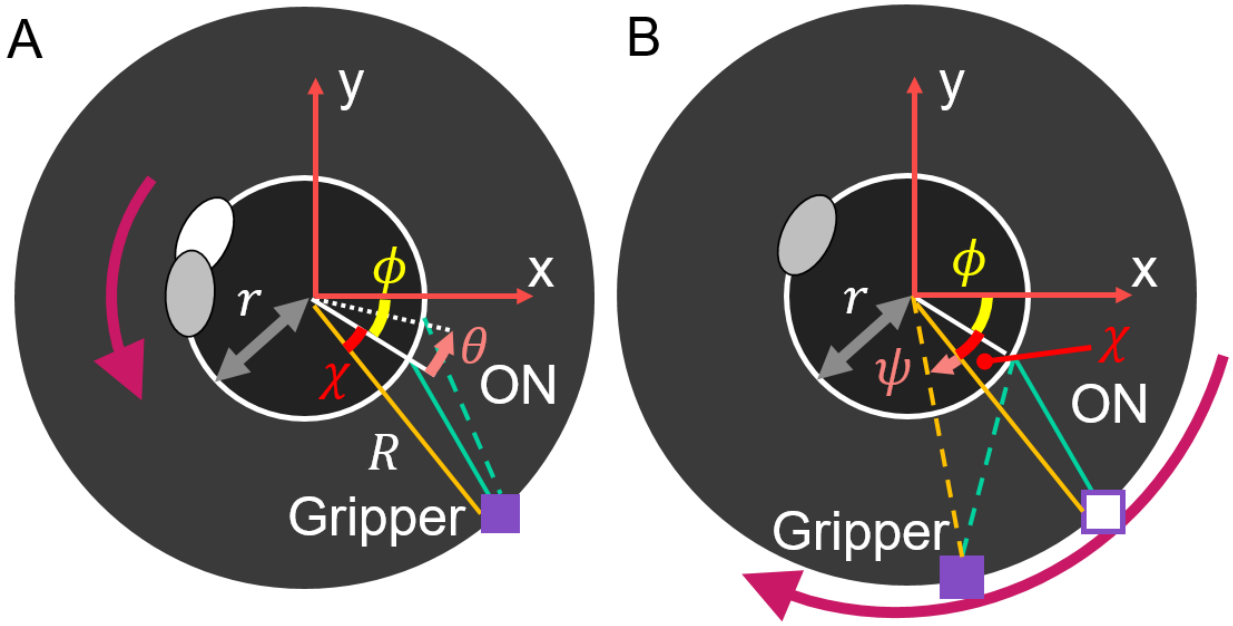

Figure 28. The detailed image for the eye holder and gripper. (A-B) schematic demonstrating equivalence between rotation of eye versus shifting the gripper along the arc. In these two panels, r represents the globe radius and ϕ the azimuth of the optic nerve junction. The location of the gripper can be specified by the distance R and the incremental angle χ, and θ a indicate the angle of rotation for the eyeball and and ψ for the gripper. The solid and dotted cyan lines correspond to the ON path at the initial and deformed configuration. Gripper angle is exaggerated in panel B for diagrammatic clarity.

Even effort to remove a maximal optic nerve length at enucleation inevitably leaves behind some optic nerve in the donor orbital apex (Fig. 29A). Without consideration of this anatomical limitation, strains on the optic nerve and sclera might be exaggerated because the lost optic nerve is replaced by a rigid metal rod. To account for this optic nerve truncation, a virtual orbital apex was employed. Consistent with published anatomy[77], the distance between the globe center and the orbital apex was set to be 41 mm, and the angle between a sagittal plane and a line from the globe center and the orbital apex was 22°. From this the coordinates of the orbital apex were computed to be $x = -41\sin 22°$, $y = -41\cos 22°$ with the globe center set as the origin. Assuming a 17° angle between the fovea and the optic disc[77], the coordinate of the center of the optic nerve junction were computed to be $x = r\sin(\omega - 17°)$, $y = -r\cos(\omega - 17°)$ where r is the eye radius and ω is the angle of rotation with respect to the sagittal plane (Fig. 29B). The straight optic nerve length l was measured with a digital caliper. Then, the initial position of the gripper tip was adjusted by referring to the virtual orbital apex and the straight optic nerve distance. The gripper tip was located over a line between the optic nerve junction and the orbital apex, while the optic nerve length was maintained as l. At the deformed configuration, the distance between the orbital apex and the optic nerve junction increases trigonometrically because of the 6° adduction, and the extension proportion of the distance can be computed (Fig. 29C). Hence, I stretched the remaining actual optic nerve by the same proportion. Because the optic nerve is stretched straight under conditions of this experiment, the extension proportion would be equivalent, while the gripper tip was on the line segment between the optic nerve junction and the virtual orbital apex.

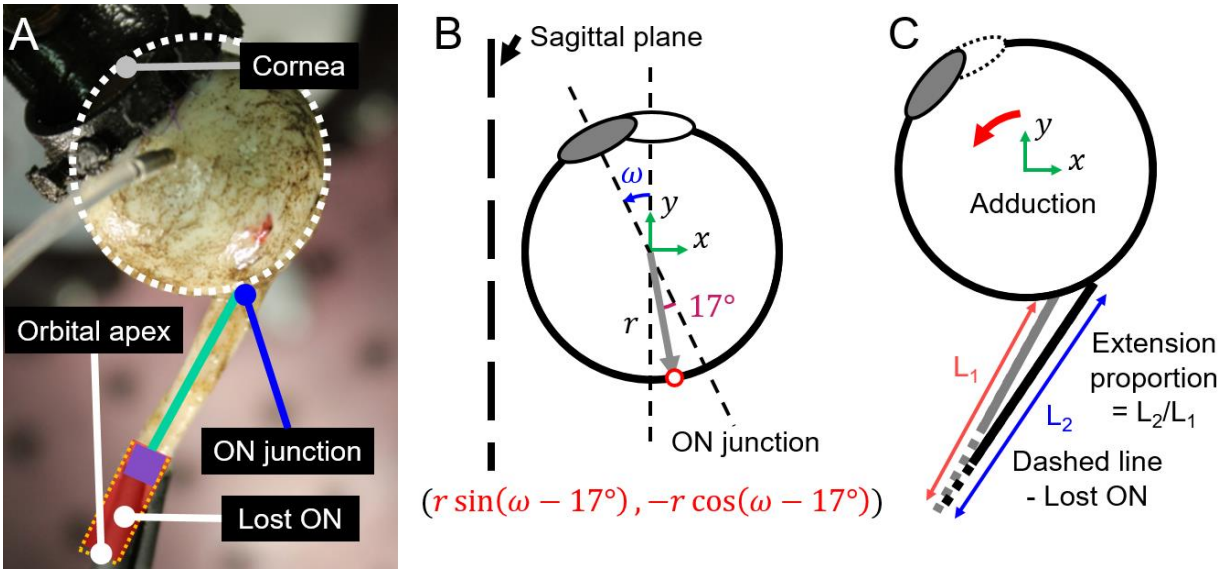

Figure 29. Schematic diagram for geometric computation. (A) Globe in eye holder with superimposed virtual orbital apex. Because of the offset between the globe center and the optic nerve junction, alignment of the optic nerve and the clamp vary slightly from collinearity. (B) Coordinates for the optic nerve junction during adduction. (C) Extension proportion of the optic nerve length during incremental adduction. Adduction angle is exaggerated in panel C for diagrammatic clarity.

3D digital image correlation analysis. The raw images were cropped into square images of 4000 by 4000 pixels by removing redundant backgrounds. Then, calibration for estimating 3D coordinates was conducted for each camera pair. By attaching a patterned paper on a cylinder of 25.4 mm diameter, I used the rod to refer to known 3D coordinates. After taking images for the rod, the regions to be used for the calibration were manually selected, and the regions for a camera pair had overlapped domains. Then image point coordinates and known 3D coordinates were matched to obtain direct linear transformation parameters for each camera (equation 2):

$$x_p = \frac{L_1X + L_2Y + L_3Z + L_4}{L_5X + L_6Y + L_7Z + 1}$$
$$y_p = \frac{L_8X + L_9Y + L_{10}Z + L_{11}}{L_5X + L_6Y + L_7Z + 1} \quad (2)$$

where $L_1, \dots, L_{11}$ are calibration parameters. Also, x_p and y_p are image point coordinates, and X, Y, and Z are known 3D coordinates on the cylindrical rod.

Similarly, regions of interest for digital image correlation were manually selected by paying attention to the overlapped regions. Because speckles were applied to the scleras, 2D digital image correlation algorithm was used to identify corresponding regions between the reference and deformed objects. By referring to the calibration parameters and 2D digital image correlation results, 3D surfaces were reconstructed via using open source 3D digital image correlation[47]. Then 3D displacements around the optic nerve junction were estimated. Since the reconstructed surfaces was tessellated by triangular faces, the estimated displacements were used to compute the surface area ratios of triangle meshes.

Tensile testing. After digital image correlation testing, each of the ocular tissues was divided into anterior, equatorial, posterior, peripapillary sclera; optic nerve; and optic nerve sheath. Except for the optic nerve, each region was dissected into rectangular strips that were used for uniaxial tensile testing[87]. The tensile load cell consisted of a linear motor (Ibex Engineering, Newbury Park, CA, USA) and a sensitive force sensor with ±0.1% error. A frictionless air bearing was also used to support the load cell and minimize errors from frictional force. Cross-sectional areas of tissues were measured by digital calipers (Mitutoyo Co., Kawasaki, Japan). Using closed feedback control, tissues were elongated until the force sensor indicated 0.02 N as the preloading condition. Then, 6 cyclic 5% preconditioning and tensile tests were performed until rupture

occurred. The loading rate was 0.07 mm/sec, and the sampling rate was 5 Hz. During the experiments, tissues were inside an environmental chamber so that the temperature was 37°C and humidity approached 100%. As a result, stress-strain curves were obtained for each tissue region after conclusion of the digital image correlation experiments. Tensile data were also used for numerical simulation.

Analysis of tensile testing results. To compute tangent moduli of ocular tissues, stress-strain curves were fitted by a polynomial curve fitting. The polynomial curve fitting was conducted by using the built-in function in MATLAB 2017b (MathWorks, Natick, MA, USA). Thus, tangent moduli were computed by differentiating the polynomial equations. For optic nerve sheath data, the bilinear regression was conducted. Two lines to have least squared errors were found for optic nerve sheath data after log transformation of stresses and strains. The intersection point between two linear lines was assumed to be the transition point.

Numerical simulation by using finite element modeling. Each geometry model was created for each specimen, consisting of the whole globe and attached optic nerve using SolidWorks 2021 (Dassault Systèmes, Vélizy-Villacoublay, France). For each eye tissue used in the experiment, the axial length and transverse diameter of a globe and the optic nerve sheath diameter at the optic nerve junction were measured, and the data were applied to the design models. The detailed dimensions are tabulated in Table 1. Local tissue regions were parameterized individually for tensile data collected for the anterior, equatorial, posterior, peripapillary scleras, lamina cribrosa, optic nerve, and optic nerve sheath. Material properties from the uniaxial tensile testing were converted to reduced polynomials models assuming isotropic and hyperelastic material behavior. Then the individualized eye models were imported in the Abaqus 2023 (Dassault Systèmes, Vélizy-Villacoublay, France) software package for finite element modeling,

and the geometries were tessellated by using 10-node second order tetrahedral meshes. A total of 540,196 ± 64,198 meshes were used because mesh convergence tests of the model have demonstrated this to be sufficient[35, 77]. The Poisson ratios of all tissues were set to be 0.495 because the tissues were assumed to be incompressible as is typically assumed for soft tissues[88]. As boundary conditions, the optic nerve and its sheath was fixed at the orbital apex, and the globe was adducted by 6° so that surface area ratios could be computed. To simulate the pre-stretch, tensile testing results of posterior regions were translated by 5% along the strain axis. Due to the pre-stretch, tissues become stiff because stress-stress curves become steep. The stiffened models were compared to models without the offset. Models with intraocular pressure elevation from 15 to 30 mmHg were also simulated for the comparison. Surface area ratios for all models were computed by using our own code. Nodal coordinates of the sclera surface at the initial and deformed configurations and connectivity of the nodes were exported by Abaqus 2023. By using the exported information, I defined triangles on the sclera surface and computed surface areas of the triangles before and after the deformation.

Statistical analysis. For the data analysis, paired t-testing, and one- and two-way ANOVA were performed by using GraphPad Prism 9 (GraphPad Software, San Diego, CA, USA). Generalized estimating equations was computed for the multivariate analysis by using IBM SPSS 25 (Armonk, NY, USA).

Results

Tensile testing. I conducted uniaxial tensile tests of postmortem human ocular tissues and plotted stress-strain curves (Fig. 30). From the individual curves, tangent moduli to represent stiffness were computed. At 3% strains, tangent moduli of anterior, equatorial, posterior, and

peripapillary scleras were 13.96 ± 3.37 MPa, 11.73 ± 3.54 MPa, 7.01 ± 2.90 MPa, and 2.34 ± 1.19 MPa, respectively. The tangent moduli of optic nerves and optic nerve sheaths at 3% strains were 0.90 ± 0.56 MPa and 1.28 ± 0.50 MPa. When the strains reached 7%, tangent moduli of anterior, equatorial, posterior, and peripapillary scleras were 22.6 ± 6.6 MPa, 22.2 ± 5.4 MPa, 10.2 ± 4.8 MPa, and 3.2 ± 1.5 MPa, respectively. Also, the tangent moduli of optic nerves and optic nerve sheaths were 1.39 ± 0.61 MPa and 3.0 ± 1.3 MPa at 7% strains.

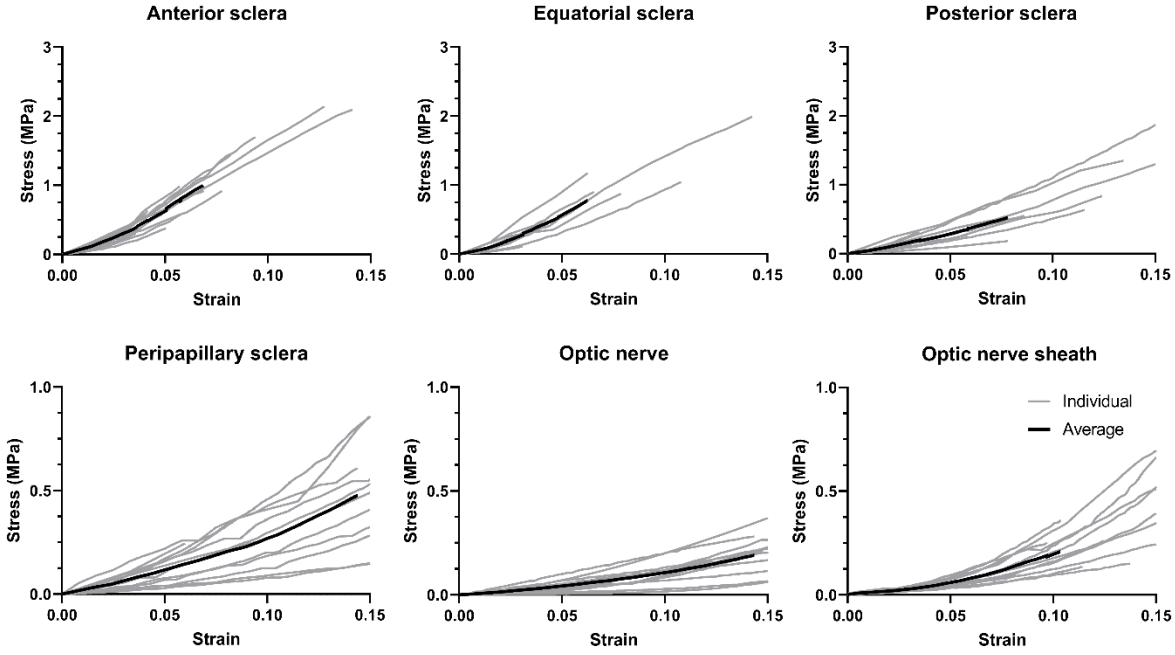

Figure 30. Tensile testing results for 12 human postmortem eyes. Individual (gray) and average (black) engineering stress-strain curves for scleras, optic nerves, and optic nerve sheaths. Note that the range of y-axis differs between the first and second rows.

The slope of the stress-strain curve varied with the increase of strains, and the curve had no local extremum point. Thus, I thought that the relationship between stresses and strains can be represented in a form of $\sigma \sim \varepsilon^{\gamma}$ where σ, ε, and γ correspond to stresses, strains, and a variable

exponent, respectively. Because the function form is highly influenced by the variable exponent γ, I replotted the tensile test data by using a log-log plot. For a curve of $\sigma \sim \varepsilon^{\gamma}$, the equation $\log(\sigma)=\gamma\log(\varepsilon)$ is followed by the logarithm transformation, so the slope of the log-log graph represents γ. When I plotted the log-log curves for different ocular regions, the curve from optic nerve sheaths represented two different slopes. Thus, bilinear curve fitting was used to find the transition point of the stress-strain curve for optic nerve sheaths. The goodness of fit was 0.953 in low strain region, and the value was 0.991 in high strain region. I found that the transition occurs around 3.4% strain from the uniaxial tensile testing of postmortem human optic nerve sheaths (Fig. 30).

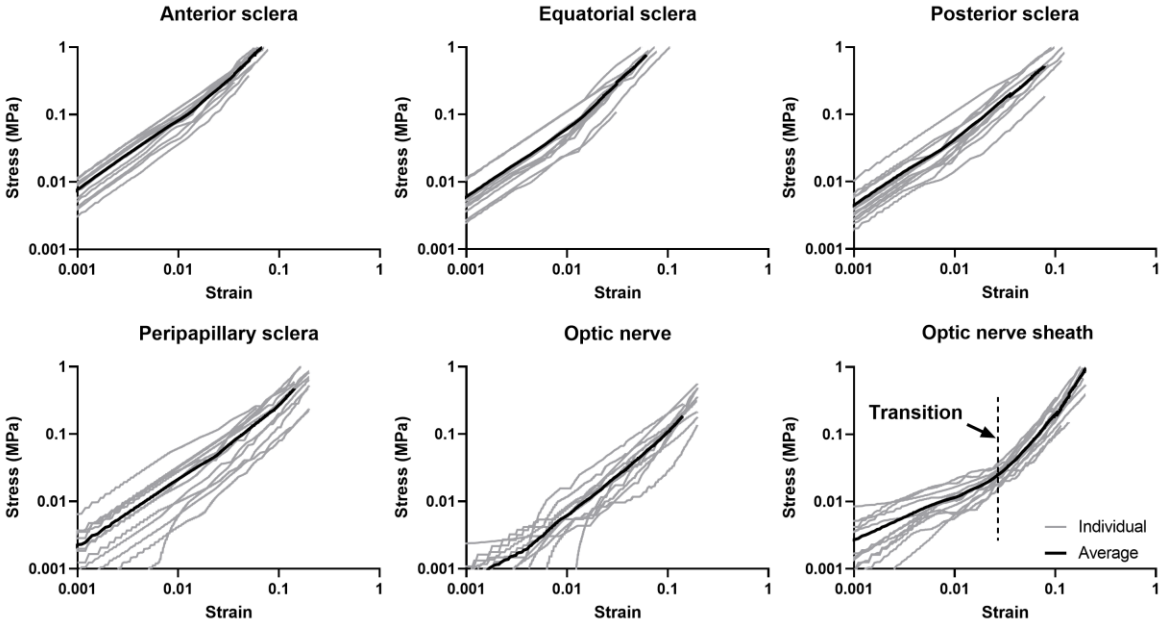

Figure 31. Log-log plots of tensile testing results for 12 human postmortem eyes. Note the change in slope of the ON sheath curve at around 3.4% strain.

Digital image correlation. By attaching a uniformly distributed pattern on the surface of a cylinder of known size, I performed the calibration for computing 3D coordinates by combining

two 2D images (Fig. 32A). Since the diameter of the cylinder was 25.4 mm, its dimension and curvature were similar to those of human eyes. The errors of 3D coordinates from each camera pair were about 10 μm.

A verification system with two pillars holding a sheet of randomly patterned paper was (Fig. 32B) placed on a vernier stage separately controlling translation in normal and tangential directions. Displacement magnitudes and surface area ratios were measured for the two translation directions (Fig. 32C and 32D). Errors did not become significant until translation exceeds 2 mm in both normal and tangential directions. Since all displacement magnitudes observed in these experiments are smaller than 2 mm, measurements can be considered reliable. Except for the reliability test, I also conducted the repeatability test by measurements of two repeated adduction events for the same eye. For the same eye, two different heat maps to represent surface area ratios were compared (Fig. 33). Average of the absolute difference between two heat map values across the domain was 0.0059.

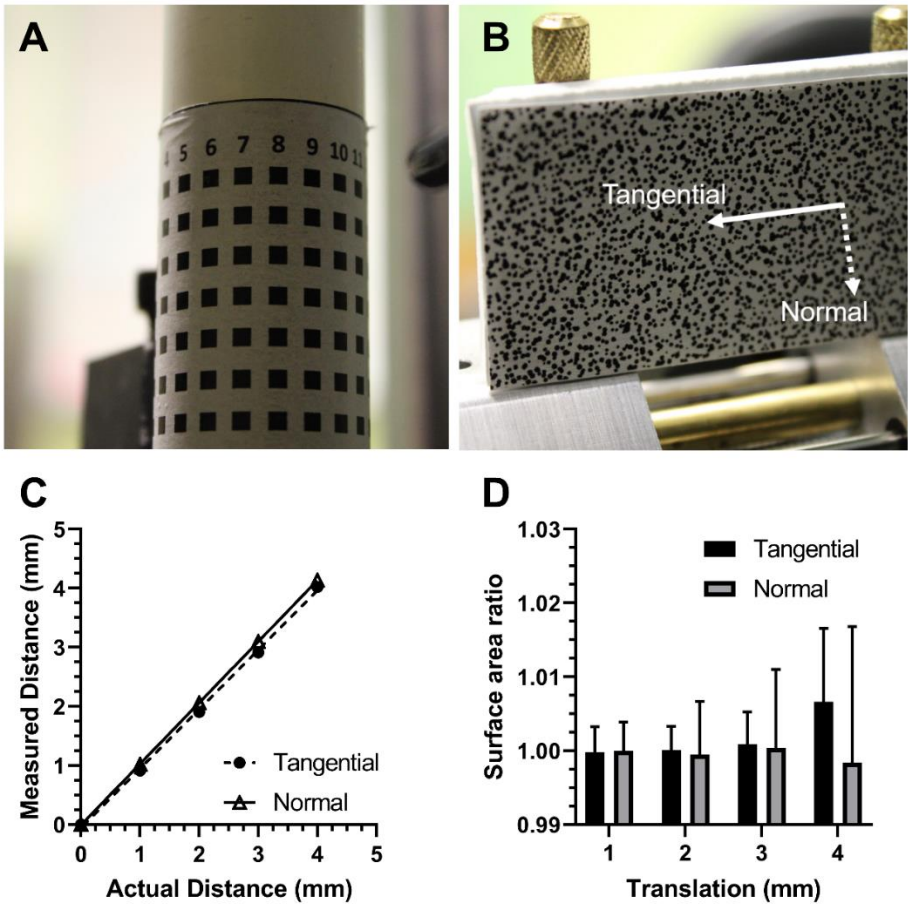

Figure 32. The verification systems for the 3D digital image correlation analysis. (A) A cylindrical rod to calibrate 3D coordinates across a cylindrical surface. (B) The mechanical system to translate the patterned paper. (C) Measured displacement magnitudes and (D) surface area ratios as functions of translation distances.

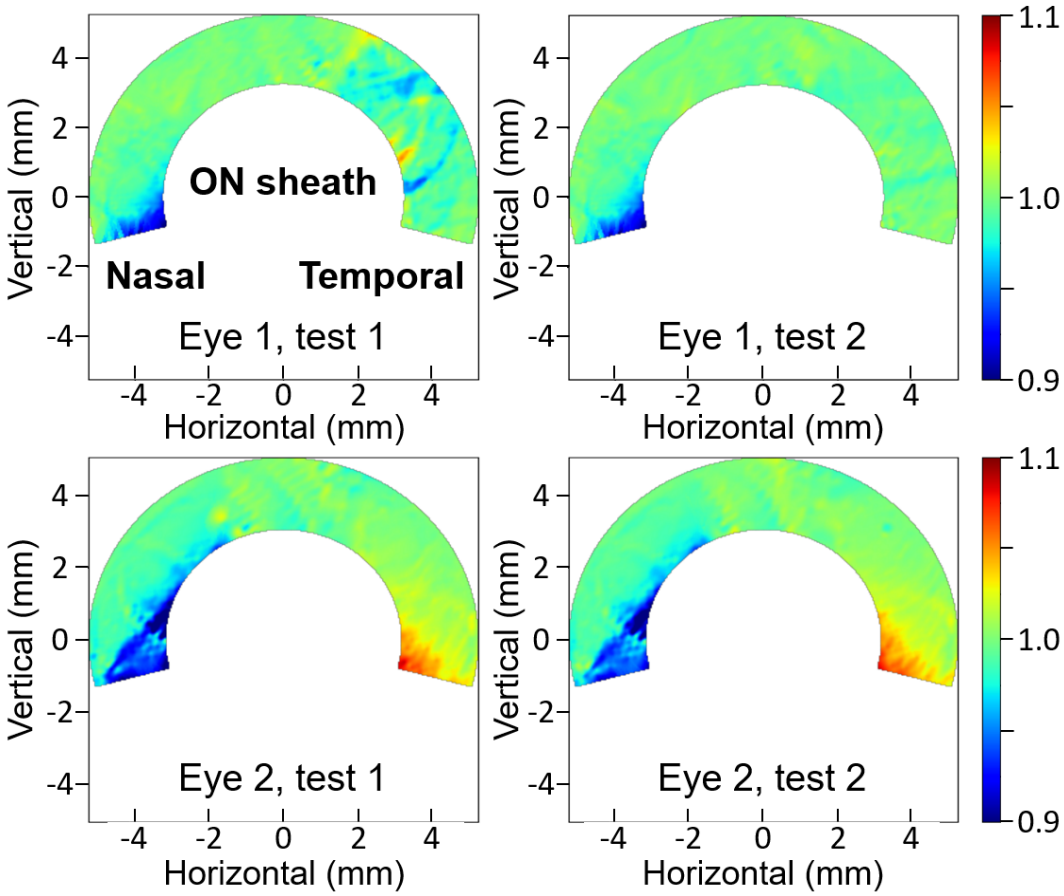

Figure 33. The repeatability test for the system. The heat maps on the same row for the surface area ratios were from the same eye tissue at different sets. (A) and (B) are from the same eye tissue, and (C) and (D) are from the same one.

After confirming the reliability and repeatability of the digital image correlation analysis, I investigated whether localized scleral deformations along three directions occur for 12 postmortem human eyes. For comparison with adduction, intraocular pressure elevation to 30 mmHg was also applied. For analysis of horizontal and vertical directions, three strips of 0.1 mm width over the sclera surface were defined along the nasal horizon, superior, and temporal horizon directions (Fig. 34A). Then surface area ratios were plotted along the strip after the intraocular pressure elevation or adduction. Surface area ratios become less than one when the local regions are compressed, and

the ratios are larger than one as the region expands. Because the region of interest was outside the optic nerve sheath, the deformation was not large. In particular, the pressure elevation from 15 to 30 mmHg did not induce any detectable deformation on the sclera outside the optic nerve sheath. For 6° incremental adduction, the sclera expanded slightly temporal to the optic nerve, whereas it was compressed nasal to the optic nerve. All deformations occurred within 2 mm of the optic disc (Fig. 34).

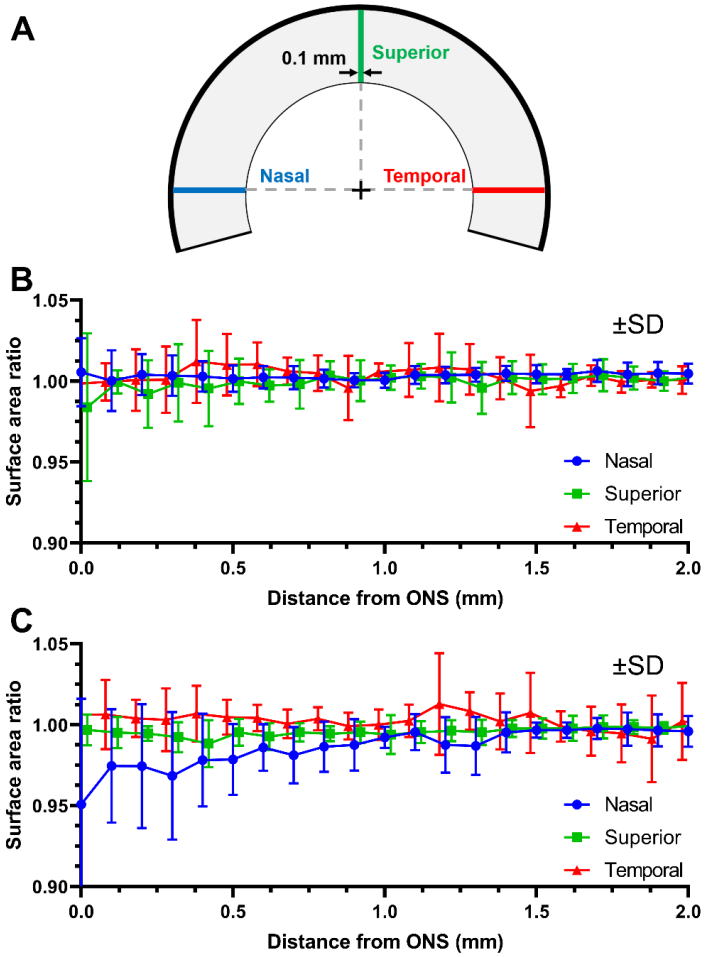

Figure 34. Surface area ratios depending on regions and distances from optic nerve sheaths. (A) The strips were defined in the sclera for analysis of changes in surface area. (B) Intraocular pressure elevation from 15 to 30 mmHg did not change scleral surface area. (C) Adduction by 6° produced changes in surface area within 1.2 mm of the nasal edge of the optic nerve sheath.

Deformation was quantified by change in local surface areas of the sclera, represented as ratios of loaded to unloaded areas in defined regions consisting of 3 fan-shaped sectors of 30° central angle in the nasal, superior, and temporal regions as diagrammed in Fig. 35A. Because the deformations were confined to within 2 mm from the optic nerve sheath (Fig. 34), each sector was divided into 2 annular regions defined by radial distances of 1 and 2 mm from the optic nerve sheath. Changes in surface area ratios were analyzed for each of the local areas defined in this way, during elevation of intraocular pressure from 15 to 30 mmHg, without altering optic nerve position (Fig. 35D).

None of the changes resulting from intraocular pressure elevation was statistically different from unity (P=0.121, paired t-test). Changes in surface area ratios caused by 6° incremental adduction were also computed (Fig. 35E). In the region 1 mm from the margin of the optic nerve sheath, the surface area ratios in the nasal region and superior regions were 0.976 ± 0.007 and 0.994 ± 0.004, respectively, but stretched to 1.003 ± 0.010 for the temporal region by adduction. The nasal region was compressed significantly within 1 mm of the optic nerve sheath by adduction (P=0.0077), but not at 2 mm. In the region 2 mm from the margin of the optic nerve sheath, the corresponding values were not distinguishable from unity at 0.992 ± 0.007, 0.996 ± 0.003, and 1.000 ± 0.006, respectively (P=0.338). To ascertain that extreme intraocular pressure elevation ultimately affects the scleral surface, we examined the case of intraocular pressure elevation to 45 mmHg for two eyes (Fig. 35F). Modest increases of surface area ratios in all of nasal, superior, and temporal regions showed that the 3D digital image correlation analysis can detect small scleral deformations caused by extreme intraocular pressure elevation.

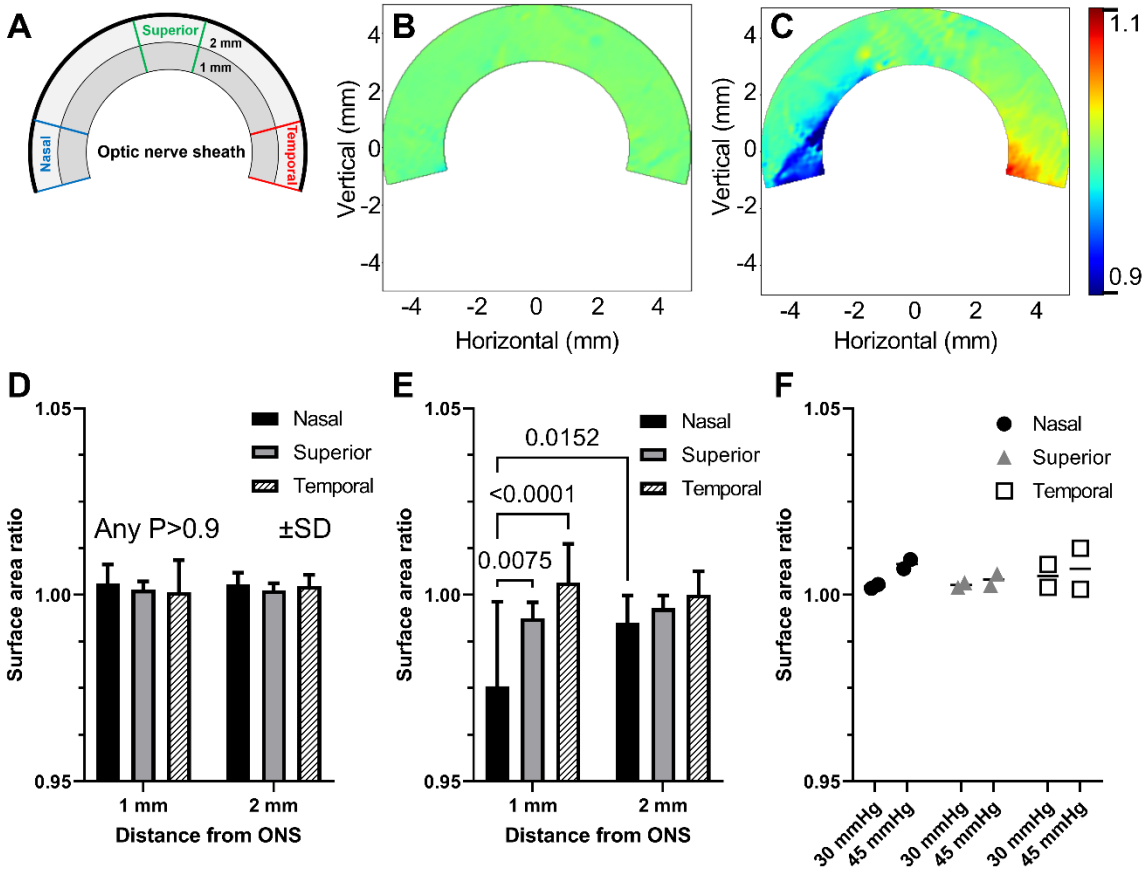

Figure 35. Surface area ratios depending on regions and mechanical stimuli. (A) The schematic diagram for how to divide the scleral region. Heat maps for the surface area ratio of one sample by: (B) intraocular pressure elevation to 30 mmHg and (C) adduction by 6°. The characterization of surface area ratios by: (D) intraocular pressure elevation to 30 mmHg and (E) adduction by 6°. (F) Comparison between intraocular pressure elevation to 30 and 45 mmHg (N=2 eyes). Two-way ANOVA was used. The error bars represent the standard deviations.

Finite element modeling. In addition to modeling the properties of each ocular tissue region as using linear stiffness, I also considered as a separate case the effect of strain stiffening in the optic nerve sheath (Fig. 31) where the optic nerve and its sheath had 5% pre-stretch at the initial

position of 26° adduction. The finite element modeling then simulated the effect of incremental adduction from 26° to 32°, with or without this pre-stretch. Because optic nerve tensile behavior of the ninth eye in Table 1 appeared to be confounded by artifact, I did not include perform an individualized finite element model for this eye. A total of 11 eye models were simulated, corresponding to each of the eyes tested by 3D digital image correlation.

For comparison of digital image correlation data with finite element modeling, the sclera was divided into 6 regions (Fig. 35A). For the 11 finite element modeling cases without the 5% pre-stretch for the optic nerve and its sheath, surface area ratios during adduction tethering in the nasal, superior, and temporal regions were computed (Fig. 36A). In case of the 5% pre-stretch models, surface area ratios were also obtained (Fig. 36B). In either case, temporal regions were strained ($P<0.0001$, paired t-test with unity). However, nasal regions were compressed only in models with the 5% pre-stretch ($P<0.01$), and they were not compressed in models without the pre-stretch ($P=0.872$). The effect of the pre-stretch on deformations in the nasal regions was reaffirmed by performing paired t-test (Fig. 36D, $P=0.0023$). Also, scleral deformations of nasal regions in models with the 5% pre-stretch were localized in the 1 mm group, and they were unnoticeable in the 2 mm group ($P=0.148$). For intraocular pressure elevation from 15 to 30 mmHg without adduction tethering, finite element modeling predicted no changes from unity in surface area ratios in any regions (Fig. 36C, $P>0.188$). For intuitive appreciation, absolute maximum principal strains are demonstrated for a 5% pre-stretched adduction model of an eye from 82 years old Caucasian man (Fig. 36E), and dimensions of the eye correspond to those of the first eye in Table 1.

The correlation between surface area ratios and other variables was investigated by generalized estimating equations. Donor age, axial length, transverse diameters, and tangent

moduli of all scleras, optic nerve, and optic nerve sheath at 3% and 7% were uncorrelated with surface area ratios (P>0.216). However, the optic nerve sheath radius was negatively correlated with the surface area ratios (P=0.046).

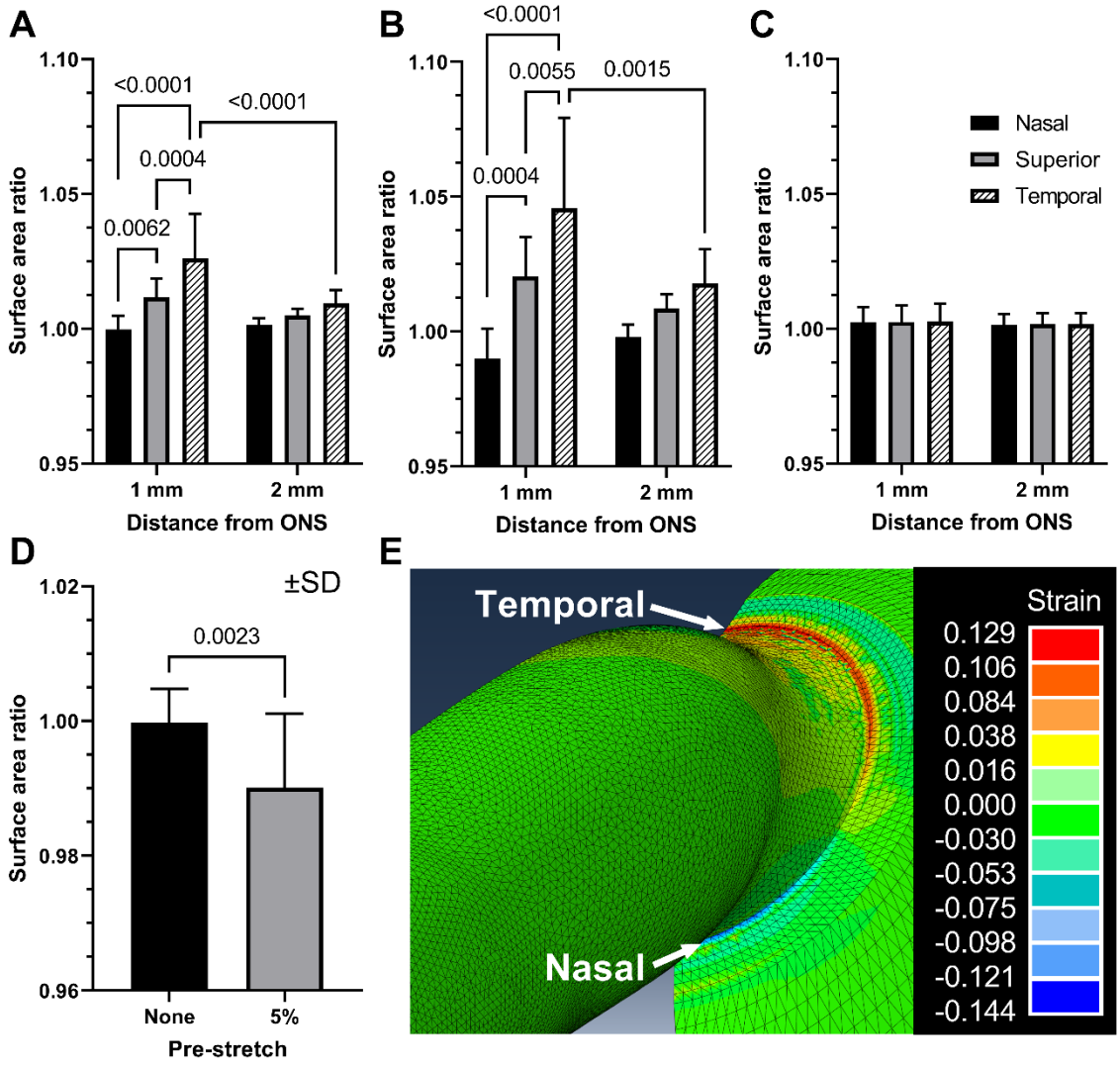

Figure 36. Surface area ratios from simulations. (A) The models without 5% pre-stretch. (B) The models with 5% pre-stretch. (C) The models with intraocular pressure elevation from 15 to 30 mmHg. (D) Surface area ratios in the 1 mm nasal region depending on the pre-stretch. (E) Visualization of absolute maximum principal strains for the adduction with 5% pre-stretch. The

error bars represent the standard deviations. For the statistical analysis, and paired t-test and two-way ANOVA were used.

The correlation between the surface area ratios from digital image correlation experiments and the eye-specific simulation models was examined (Fig. 37). Pearson's correlation coefficients for the nasal, superior, and temporal regions were 0.575, 0.095, and 0.348. Linear regression of simulated against experimental data yielded a slope of 0.295 in the nasal region, while the slope was 1.212 in the temporal region.

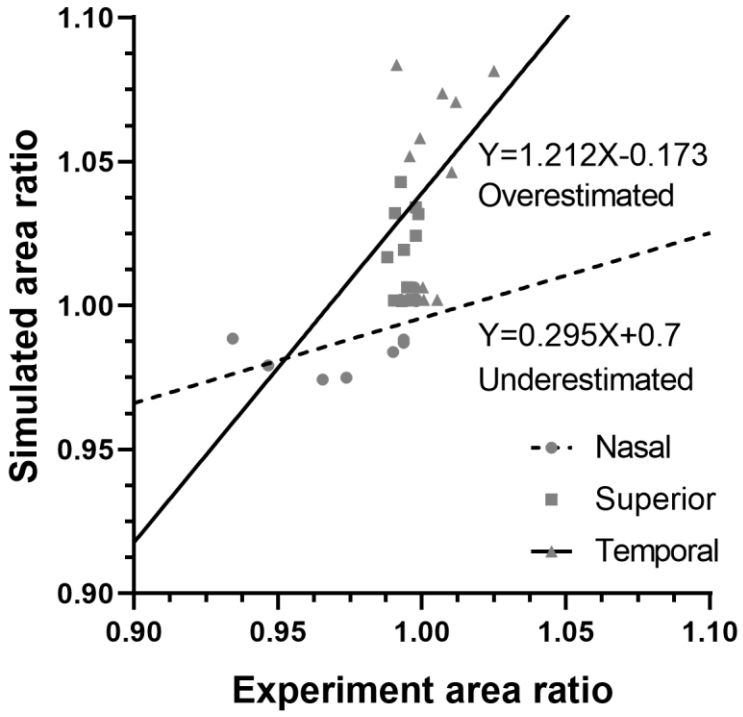

Figure 37. Correlation of observed and predicted changes in posterior scleral surface area caused by incremental adduction from 26-32° in 11 eyes. The prediction was from models with the 5% pre-stretch. Each point represents a superior, nasal, or temporal scleral region, which is far from

the optic nerve sheath border by 1 mm for each eye. Dotted line represents linear regression for the nasal sclera, while the solid line indicates linear regression for the temporal region.

Discussion

In this current study, I conducted experiments as well as numerical simulations to replicated incremental adduction from 26-32° in magnetic resonance imaging studies for living humans[17, 18]. In that situation, the optic nerve had become straightened at 26°, requiring optic nerve elongation, globe translation, and/or scleral deformation to permit the additional adduction. The current experiment in postmortem human eyes imaged by 3D digital image correlation from a posterior perspective the sclera where it joins with the optic nerve and its sheath. Replicating the in vivo experiment, adduction from 26° to 32° during optic nerve tethering compressed the sclera adjacent to the nasal side of its junction with the optic nerve sheath, while stretching the adjacent sclera on the temporal side. There was little effect on the superior sclera. The scleral deformations were greatest adjacent to the optic nerve sheath but propagated at most to about 2 mm beyond it. While adduction with the optic nerve tethered generated significant scleral deformations, none were detectable during intraocular pressure elevation to 30 mmHg. The absence of observed effect of moderate intraocular pressure elevation does not indicate insensitivity of the method, because extreme intraocular pressure elevation to 45 mmHg did detectably stretch the sclera on the nasal, temporal, and superior border of the optic nerve sheath. Individualized finite element models assembled for each eye using tensile properties measured in the optic nerve, optic nerve sheath, and local regions of sclera for that eye predicted change in regional scleral surface area ratio based on these individualized finite element models during the adduction loading. These changes correlated significantly with those observed by 3D digital image correlation, while also predicting

the observed absence of effect of intraocular pressure elevation. However, performance of finite element modeling was better when material parameterization of the optic nerve sheath included the effect of pre-stretching.

Comparison between adduction tethering and intraocular pressure elevation requires a nuanced approach. Adduction tethering generated larger deformations of the posterior scleral surface than intraocular pressure elevation, but this perspective is unusual insofar as most other studies of the effect of intraocular pressure elevation have reported on intraocular effects on the disc and peripapillary tissues in normal and glaucomatous eyes[86]. Even so, since in this study the main driver of intraocular peripapillary deformations was traction by the optic nerve and its sheath, the current findings support previous simulations of adduction that concluded that deformations of lamina cribrosa by adduction are at least at great as those due to intraocular pressure elevation[16, 77].

In addition to being individually variable among donors of various ages, tensile properties of ocular tissues may depend on experimental conditions such as strain rates[89] and stress levels[90], I compared our results with previous reports[81, 87, 90-95]. Although there are variations among human sclera data[87, 90-92, 94], tangent moduli at low and high stresses were usually ~10 MPa [90, 91, 94] and >20 MPa[87, 90, 92, 94]. In case of human peripapillary sclera, reported tangent moduli were less than 10 MPa[87, 93, 95]. Mechanical properties of peripapillary sclera have often been estimated by the inverse finite element method[86, 93]. Though direct comparisons with this different methodology must necessarily be limited, the published values have the same order of magnitude as ours. The uniaxial tensile data for the human peripapillary sclera reported 8.6 MPa for the tangent modulus at 7% strain[87], which is higher than the modulus in this current study. The peripapillary sclera was tested in a 7.5 mm in diameter annular region in the current study, limiting the specimen aspect

ratio to about 2, although aspect ratio would preferably exceed 5 for uniaxial tensile[96]. The lamina cribrosa has been elsewhere estimated to have a modulus of 0.3 MPa[81], and this value is comparable to the tangent moduli of the optic nerve in this study. In case of the human optic nerve sheath, a previously reported tangent modulus at 7% was 11.5 MPa[87], and the preload of 0.05 N was applied in the previous study. The preload in the current study was 0.02 N, so preload might account for some difference in observed toe regions.

Based on optical coherence tomography analysis[13], 26° adduction approximates a threshold above which deformation of the disc and peripapillary tissues increases abruptly. This angle has been interpreted as the threshold at which the formerly sinuous optic nerve exhausts its path redundancy and becomes straight[77]. However, tension in the optic nerve and its sheath produced by further adduction past 26° would also depend upon its stress-strain curve after straightening. The current tensile tests illustrate an important nonlinearity causing optic nerve sheath stiffness to increase appreciably beyond 3.4% strain, a behavior that represents strain stiffening[82, 83]. To ascertain if the transition could occur in adduction, I calculated optic nerve strain due to 26° adduction. The mean radius of human eyes is 12 mm[97], and the distance between the globe center and the orbital apex is 41 mm[77]. Also, the angle between a sagittal plane and a line from the globe center and the orbital apex is 22°. Then the coordinate of the orbital apex is $(-41\sin 22°, -41\cos 22°)$ when the globe center is the origin. Assuming that the angle between the fovea and the optic disc is 17°[77], the coordinate of the optic nerve junction was $(12\sin(\omega - 17°), -12\cos(\omega - 17°))$ where ω is the angle of rotation with respect to the sagittal plane. As a result, the optic nerve and its sheath are elongated by 7.5% at 26° adduction if globe translation is negligible. Accounting for observed nasal and posterior globe translation of 0.2 mm in normal subjects[98], the optic nerve and its sheath are strained by 6.6% when the eye is adducted

by 26°. On the other hand, the optic nerve path is actually sinuous in central gaze, and its path is about 3% longer than the straight path from the orbital apex to the globe[17, 18]. Accounting for the initial 3% average optic nerve path redundancy from magnetic resonance imaging, the redundancy of the sinuous optic nerve path would be exhausted before adduction reaches 26°. Since incremental adduction would induce strain in the optic nerve and its sheath after the optic nerve path becomes straight, the optic nerve and its sheath would be stretched by 3.6% when adduction reaches 26°, the starting point of the current 3D digital image correlation experiment. Intriguingly, the strain value of the optic nerve and its sheath at 26° adduction was close to the transition point of stress-strain curve of human optic nerve sheath. This calculation suggests that strain stiffening of the optic nerve sheath can occur during adduction within the physiological range, and 26° adduction angle might represent the beginning of strain stiffening of the optic nerve sheath, rather than the threshold of optic nerve straightening. This consideration justifies the inclusion of pre-stretch in the finite element modeling performed here. Of course, the foregoing analyses assume average anatomical dimensions and average tissue properties. It has been noted elsewhere that mechanical effects of adduction may be exaggerated when anatomical or tissue material property combinations are unfavorable[77].

Through a similar computation, I attempted to predict the adduction angle where the optic nerve path would become straight. The averaged coordinate of the orbital apex is $(-41\sin 22°, -41\cos 22°)$, and the averaged coordinate of the optic nerve junction is $(-12\sin 17°, -12\cos 17°)$ in central gaze. Then the straight distance between the orbital apex and the optic nerve junction is 29.06 mm. On the other hand, because magnetic resonance imaging was conducted in supine position[17, 18], the gravitational field might influence anteroposterior locations of eyeballs during magnetic resonance imaging. Assuming that the globe was posteriorly

translated by 0.1 mm during image acquisition, the shortest distance between the orbital apex and the optic nerve junction would be 28.97 mm at that moment. Considering the initial 3% average optic nerve path redundancy[17, 18], the total length of the intraorbital optic nerve would be 29.84 mm. The distance between the orbital apex and the optic nerve junction at 14° adduction would be 29.83 mm when the posterior globe translation of normal subjects is 0.09 mm[98]. As a result, I speculate that this 14° angle might be a threshold of optic nerve straightening. If so, optic nerve tethering might be a more common phenomenon in daily life as it could be associated with smaller adduction angles that are more commonly attained.

The results from this study imply potentially pathological significance of adduction tethering for the optic disc and peripapillary region. Scleral deformations caused by optic nerve and sheath traction in adduction are concentrated focally at the optic nerve junction and propagate only 1-2 mm from the edge of the sheath on the exterior scleral surface. However, at the external surface, the ON sheath diameter is much larger than the roughly 1.5 mm diameter of the optic disc internal to the eye. In fact, deformations of the disc, peripapillary vessels, and choroid observed intraocularly by confocal scanning laser ophthalmoscopy[14, 74] and optical coherence tomography[51, 62, 71] during horizontal duction occur largely within the region covered on the exterior surface by the optic nerve sheath, and so invisible to the current technique. This internal region, which includes the lamina cribrosa, is the site of optic nerve damage in primary open angle glaucoma, the world's largest cause of untreatable blindness[99, 100]. Although intraocular pressure was previously believed to be the cause of primary open angle glaucoma, elevated intraocular pressure is no longer definitional of the disease. Many patients, especially Asians[101-104], do not have abnormally elevated intraocular pressure[105], and experience optic nerve damage despite normal intraocular pressure[106], as is the case in 30-39% of whites[107-109], 57% of Blacks[110], 70% of

Chinese[111], and 92% of Japanese[102]. However, even treatment to reduce intraocular pressure does not arrest progressive optic neuropathy[112], so about 20% of patients suffer more optic nerve damage 5 years after 30% intraocular pressure reduction from normal[106], even when intraocular pressure is reduced so much that its insufficiency causes visual loss by other mechanisms[113]. Causes of glaucoma independent of intraocular pressure have been proposed to include the gradient across the lamina cribrosa of intraocular pressure against intracranial pressure[114-117] or abnormal blood flow in the disc or optic nerve[118], yet there remains no clear etiology of primary open angle glaucoma[106]. Studies have found no relationship between translaminar pressure and glaucoma[119], even varying gravitational posture[120]. Eye-movement related deformation has been proposed as another mechanical etiology for primary open angle glaucoma operating alternatively or in addition to intraocular pressure[10, 16, 76]. While the healthy optic nerve stretches during adduction tethering, in primary open angle glaucoma the optic nerve fails to stretch, abnormally retracts the globe[18], and exaggerates strain on the disc[78]. Deformations of the disc and Bruch's membrane produced by eye movements exceed intraocular pressure-related deformations suggested as pathological to retina[121], and many-fold those resulting from extreme intraocular pressure elevation[122]. Based on finite element modeling, Wang et al. predicted that 13° abduction induces larger stains of optic nerve head than intraocular pressure of 50 mmHg does[15]. Consistent with the current findings, the optical coherence tomography study of Chuangsuwanich et al. reported that adduction induced larger optic nerve head strains for patients with normal tension glaucoma than for glaucoma patients with elevated intraocular pressure[78]. A population-based study in Korea found that untreated large angle esotropia, which augments adduction, increases the primary open angle glaucoma risk at least seven-fold more than elevated intraocular pressure, while divergent strabismus does not[123]. It has further been proposed that deformations of the scleral

flange due to eye movement might lead to choroidal degeneration observed in glaucoma[124]. If eye movements do drive optic nerve pathology in primary open angle glaucoma, therapeutic alternative to medical and surgical intraocular pressure reduction might eventually be considered.

Limitations

In this current study, there were several limitations to require discussion. For the simulation model, I assumed that all the ocular tissues are isotropic. However, the peripapillary sclera is structurally anisotropic in a manner reflected in several prior finite element modeling studies[125], although no directionally selective or biaxial experimental tensile data are available to characterize this small region. Because a significant portion of fibers in the peripapillary sclera are circumferentially oriented[95, 126], the deformations in the peripapillary sclera during adduction tethering may have been underestimated for adduction. Also, though I employed the characteristic dimensions such as axial length and transverse diameter to define the geometries of eye models, they may not fully describe the realistic geometry. Additionally, the reported thicknesses of the nasal and temporal peripapillary scleras differed[86]. Nevertheless, in the current study, the finite element models assumed equal thickness for both the nasal and temporal peripapillary sclera. The finite element models did not include internal structures such as choroid and retina; these structures are much softer than sclera, so probably contribute little to externally visible scleral behavior.

The mechanical system for this current study does not reflect certain features of orbital anatomy. Firstly, the mechanical system does not consider the globe translation during eye rotation. However, translation effects might not be significant because anteroposterior and lateral globe translation in normal subjects are close to zero for adduction from 26° to 32°[98]. Second, the optic nerve length was unavoidably truncated when the eyes were enucleated. Thus, I considered the

hypothetical orbital apex to compute eye rotation and to compensate for the lack of the optic nerve length. Without such considerations, mechanical deformations on the eyeball might be exaggerated. Third, the orbital fat was not involved in the eye rotation system. Although the orbital fat usually slides like a fluid near the optic nerve, Tenon's fascia, vessels, nerves and orbital fat posterior to the eye are likely to impose mechanical loading on the ocular surface[127], potentially dissipating the energy not included in the model, so the mechanical deformations observed here might be overestimated. However, since the shear modulus of orbital fat is low[128], the shearing effects on posterior sclera might not be significant. Fourth, suturing of an eye to an aluminum eye holder might induce force on sclera anteriorly. As a result, the sclera might have been stretched, but the effects would decay in the posterior region. Since the region of interest was far from the anterior sclera, the resulting effects might not be significant. Lastly, postmortem changes of the ocular tissues may influence biomechanical behavior of the tissues.

CHAPTER 6. CONCLUSIONS

6.1. Summary

According to the optic nerve traction hypothesis, large eye rotation results in a substantial force on posterior ocular tissues, and the mechanical loads are supposed, upon numerous repetition, to be capable of inducing damage to ocular tissues. I systematically and rigorously designed a set of research studies to verify the hypothesis by empirical approaches from the perspective of solid mechanics. I ascertained that eye rotation deforms the retina layers by using scanning laser ophthalmoscopy. I showed that the direction of the driving force is toward the posterior ocular region using optic coherence tomography angiography. Moreover, magnetic resonance imaging confirmed that the driving traction force is generated by the optic nerve and its sheath during horizontal duction. Lastly, I investigated whether the driving force from the optic nerve and its sheath can be significantly transferred to the eyeball by using numerical simulation and an *ex vivo* experiment based on 3D digital image correlation analysis. The validation and quantification of the optic nerve tethering might garner support among researchers for the concept of optic nerve traction, and encourage the participation of other researchers who are familiar with downstream pathological pathways activated by mechanical stimuli.

6.2. Open research questions

Although the optic nerve tethering theory has been validated throughout this dissertation, a putative relationship between optic nerve tethering and ocular diseases such as glaucoma and myopia remains elusive. Since the optic nerve tethering was proposed as an etiology for normal

pressure glaucoma, a detailed causal relation needs to be elucidated in order to persuade other researchers. In the previous optical coherence tomography analysis, lamina cribrosa of normal tension glaucoma patients deform more than that of high tension glaucoma patients when an eye is 20° adducted[78]. The large deformation of the lamina cribrosa for normal tension glaucoma is intriguing because this result may be related to the adduction-induced optic neuropathy. However, optic discs of young adults exhibited larger deformations than those of old adults during adduction[74], so magnitudes of deformations may not be an optimal quantity to investigate glaucoma with normal intraocular pressure because this quantity can be large even for healthy young subjects. On the other hand, the mechanical property of the lamina cribrosa can be estimated by virtual fields method *in vivo*[129]. By the force balance equation at the equilibrium, the following equation can be derived.

$$\int_V \sigma : \varepsilon \, dV = \int_S T \cdot u \, dS \tag{3}$$

where σ, ε, V, T, u, and S represent the Cauchy stress, strain, the tissue volume, the external traction force, displacement, and the tissue boundary surface, respectively. When the intraocular pressure is under control, the external traction force can be replaced by the intraocular pressure level. Displacements and strains can be computed using digital volume correlation[57] for optical coherence tomography images. Once a constitutive equation for the lamina cribrosa is determined, stress can be explicitly represented a function of strains and parameters to reflect the hyperelasticity. In the literature[129], the lamina cribrosa was regarded as a neo-Hookean hyperelastic material as follows.

$$\sigma = \frac{\mu}{J}(B - I) + pI \tag{4}$$

where σ, μ, J, B, I, and p represent the stress, the shear modulus, the determinant of the deformation gradient tensor, the left Cauchy-Green deformation tensor, the identity matrix, and the hydrostatic pressure, respectively. I speculate that the authors used the isotropic neo-Hookean model because it involves only one parameter μ in the equation. With one equation, the number of unknown variables needs to be one for finding the solution. However, I anticipate that the number of equilibrium equations could increase when the intraocular pressure is controlled at two or more different levels for the same eyes. Consequently, the constitutive equation could be more sophisticated to reflect more realistic properties. Moreover, strains of the lamina cribrosa during adduction can be computed using digital volume correlation for optical coherence tomography images. Therefore, the computation of stresses in the lamina cribrosa may be feasible during adduction. Using this methodology, it would be interesting to investigate whether the stress level on the lamina cribrosa in the normal tension glaucoma is higher than that in high tension glaucoma or healthy subjects. If there is an evident correlation between the estimated stress level and ocular diseases, the research results may garner attention from other researchers and clinicians. Then, another question can be about the downstream pathways. Mechanical stimuli can induce apoptosis of retinal ganglion cells[130, 131], so both elevated hydrostatic pressure and optic nerve tethering may trigger the pathway. However, amplitude and frequency of the mechanical stimuli differ between the pressure elevation and eye movement. Given the fact that types[132], amplitude[133], and frequency[134] of mechanical stimulus affects behaviors of other cells, effects of the mechanical parameters may need to be studied accordingly.

6.3. Epilogue

The hypothesis regarding the optic nerve traction was proposed in 2016[10], but its empirical validation and quantification have not been fully explored. Although there are still open research questions, at least I can argue that the optic nerve tethering has been experimentally validated by these sequential projects. The remaining tasks would be to perform the research to address the research questions and to link the mechanical phenomena to ocular diseases such as normal tension glaucoma and myopia.

References

1. Yuhas PT, Roberts CJ. Clinical ocular biomechanics: Where are we after 20 years of progress? *Curr Eye Res*. 2023;48:89-104.

2. Girard MJ, Dupps WJ, Baskaran M, et al. Translating ocular biomechanics into clinical practice: Current state and future prospects. *Curr Eye Res*. 2015;40:1-18.

3. Kling S, Hafezi F. Corneal biomechanics–a review. *Ophthalmic Physiol Opt*. 2017;37:240-252.

4. Buzard KA. Introduction to biomechanics of the cornea. *J Refract Surg*. 1992;8:127-138.

5. Tomeo-Reyes I, Ross A, Clark AD, Chandran V. A biomechanical approach to iris normalization. *International Conference on Biometrics*. Phuket, Thailand, 2015;9-16.

6. Karimi A, Rahmati SM, Grytz RG, Girkin CA, Downs JC. Modeling the biomechanics of the lamina cribrosa microstructure in the human eye. *Acta Biomater*. 2021;134:357-378.

7. Behkam R, Kollech HG, Jana A, et al. Racioethnic differences in the biomechanical response of the lamina cribrosa. *Acta Biomater*. 2019;88:131-140.

8. McBrien NA, Jobling AI, Gentle A. Biomechanics of the sclera in myopia: Extracellular and cellular factors. *Optom Vis Sci*. 2009;86:E23-E30.

9. Boote C, Sigal IA, Grytz R, et al. Scleral structure and biomechanics. *Prog Retin Eye Res*. 2020;74:100773.

10. Demer JL. Optic nerve sheath as a novel mechanical load on the globe in ocular duction. *Invest Ophthalmol Vis Sci*. 2016;57:1826-1838.

11. Guitton D, Volle M. Gaze control in humans: Eye-head coordination during orienting movements to targets within and beyond the oculomotor range. *J Neurophysiol*. 1987;58:427-459.

12. Wu C-C, Kowler E. Timing of saccadic eye movements during visual search for multiple targets. *J Vis*. 2013;13:11-11.

13. Suh SY, Le A, Shin A, Park J, Demer JL. Progressive deformation of the optic nerve head and peripapillary structures by graded horizontal duction. *Invest Ophthalmol Vis Sci*. 2017;58:5015-5021.

14. Le A, Chen J, Lesgart M, et al. Age-dependent deformation of the optic nerve head and peripapillary retina by horizontal duction. *Am J Ophthalmol*. 2020;209:107-116.

15. Wang X, Rumpel H, Lim WEH, et al. Finite element analysis predicts large optic nerve head strains during horizontal eye movements. *Invest Ophthalmol Vis Sci*. 2016;57:2452-2462.

16. Wang X, Fisher LK, Milea D, Jonas JB, Girard MJ. Predictions of optic nerve traction forces and peripapillary tissue stresses following horizontal eye movements. *Invest Ophthalmol Vis Sci*. 2017;58:2044-2053.

17. Demer JL, Clark RA, Suh SY, et al. Optic nerve traction during adduction in open angle glaucoma with normal versus elevated intraocular pressure. *Curr Eye Res*. 2020;45:199-210.

18. Clark RA, Suh SY, Caprioli J, et al. Adduction-induced strain on the optic nerve in primary open angle glaucoma at normal intraocular pressure. *Curr Eye Res*. 2021;46:568-578.

19. Selhorst JB, Chen Y. The optic nerve. *Semin Neurol*. 2009;29:029-035.

20. Lacey H, Oliphant H, Smith C, Koenig M, Rajak S. Topographical anatomy of the annulus of Zinn. *Sci Rep*. 2022;12:1064.

21. Chalakkal RJ, Abdulla WH, Hong SC. Fundus retinal image analyses for screening and diagnosing diabetic retinopathy, macular edema, and glaucoma disorders. In: Ayman S. El-Baz, Jasjit S. Suri, eds. *Diabetes and Fundus OCT*. Amsterdam: Elsevier; 2020:59-111.

22. Jonas JB, Berenshtein E, Holbach L. Anatomic relationship between lamina cribrosa, intraocular space, and cerebrospinal fluid space. *Invest Ophthalmol Vis Sci*. 2003;44:5189-5195.

23. Downs JC, Girkin CA. Lamina cribrosa in glaucoma. *Curr Opin Ophthalmol*. 2017;28:113.

24. Sigal IA, Wang B, Strouthidis NG, Akagi T, Girard MJ. Recent advances in OCT imaging of the lamina cribrosa. *Br J Ophthalmol*. 2014;98:ii34-ii39.

25. Sigal IA, Ethier CR. Biomechanics of the optic nerve head. *Exp Eye Res*. 2009;88:799-807.

26. Yan D, Coloma F, Metheetrairut A, et al. Deformation of the lamina cribrosa by elevated intraocular pressure. *Br J Ophthalmol*. 1994;78:643-648.

27. Lee EJ, Kim T-W, Weinreb RN, Kim H. Reversal of lamina cribrosa displacement after intraocular pressure reduction in open-angle glaucoma. *Ophthalmology*. 2013;120:553-559.

28. Liu I-S. *Continuum mechanics*. Berlin: Springer; 2002:1-30.

29. Mises Rv. Mechanik der festen körper im plastisch-deformablen zustand. *Nachr Ges Wiss Göttingen, Math-Phys Kl*. 1913;1913:582-592.

30. Barnes HA. The yield stress—a review or ‘παντα ρει’—everything flows? *J Nonnewton Fluid Mech*. 1999;81:133-178.

31. Lemaitre J, Chaboche J-L. *Mechanics of solid materials*. Cambridge: Cambridge university press; 1994:37-68.

32. Özkaya N, Leger D, Goldsheyder D, et al. Mechanical properties of biological tissues. *Fundamentals of biomechanics: equilibrium, motion, and deformation*. New York: Springer; 2017:361-387.

33. Safa BN, Santare MH, Elliott DM. A reactive inelasticity theoretical framework for modeling viscoelasticity, plastic deformation, and damage in fibrous soft tissue. *J Biomech Eng*. 2019;141:021005.

34. Nikishkov G. Introduction to the finite element method. *University of Aizu*. 2004;1-70.

35. Jafari S, Lu Y, Park J, Demer JL. Finite element model of ocular adduction by active extraocular muscle contraction. *Invest Ophthalmol Vis Sci*. 2021;62:1-1.

36. Hartmann S. A remark on the application of the Newton-Raphson method in non-linear finite element analysis. *Comput Mech*. 2005;36:100-116.

37. Hu Z, Wang X, Liu Q, Paulus Y. Photoacoustic imaging in ophthalmology. *Int J Ophthalmol Eye Sci*. 2015;3:126-132.

38. Fanea L, Fagan AJ. Magnetic resonance imaging techniques in ophthalmology. *Mol Vis*. 2012;18:2538.

39. Wyawahare MV, Patil PM, Abhyankar HK. Image registration techniques: An overview. *Int J Signal Process Image Process Pattern Recognit*. 2009;2:11-28.

40. Minaee S, Boykov Y, Porikli F, et al. Image segmentation using deep learning: A survey. *IEEE Trans Pattern Anal Mach Intell*. 2021;44:3523-3542.

41. Liu X, Song L, Liu S, Zhang Y. A review of deep-learning-based medical image segmentation methods. *Sustainability*. 2021;13:1224.

42. Li Z, Liu F, Yang W, Peng S, Zhou J. A survey of convolutional neural networks: Analysis, applications, and prospects. *IEEE Trans Neural Netw Learn Syst*. 2021;33:6999-7019.

43. Teed Z, Deng J. RAFT: Recurrent all-pairs field transforms for optical flow. In: Vedaldi A, Bischof H, Brox T, Frahm JM, eds. *Computer Vision – ECCV 2020*. Cham: Springer; 2020:402-419.

44. Hur J, Roth S. Optical flow estimation in the deep learning age. In: Noceti N, Sciutti A, Rea F, eds. *Modelling Human Motion: From Human Perception to Robot Design*. Cham: Springer; 2020: 119-140.

45. Pan B. Digital image correlation for surface deformation measurement: Historical developments, recent advances and future goals. *Meas Sci Technol*. 2018;29:082001.

46. Wang G, Zhang L, Yao X. StrainNet-3d: Real-time and robust 3-dimensional speckle image correlation using deep learning. *Opt Lasers Eng*. 2022;158:107184.

47. Solav D, Moerman KM, Jaeger AM, Genovese K, Herr HM. MultiDIC: An open-source toolbox for multi-view 3D digital image correlation. *IEEE Access*. 2018;6:30520-30535.

48. Kim TK. T test as a parametric statistic. *Korean J Anesthesiol*. 2015;68:540-546.

49. Owusu-Darko I, Adu IK, Frempong NK. Application of generalized estimating equation (GEE) model on students' academic performance. *Appl Math Sci*. 2014;8:3359-3374.

50. Huang J, Huang J, Chen Y, Ying G-s. Evaluation of approaches to analyzing continuous correlated eye data when sample size is small. *Ophthalmic Epidemiol*. 2018;25:45-54.

51. Chang MY, Shin A, Park J, et al. Deformation of optic nerve head and peripapillary tissues by horizontal duction. *Am J Ophthalmol*. 2017;174:85-94.

52. Bay H, Tuytelaars T, Van Gool L. SURF: Speeded up robust features. In: Leonardis, A, Bischof H, Pinz A, eds, *Computer Vision – ECCV 2006*. Berlin: Springer; 2006:3951:404-417.

53. Azad R, Asadi-Aghbolaghi M, Fathy M, Escalera S. Attention deeplabv3+: Multi-level context attention mechanism for skin lesion segmentation. In: Bartoli A, Fusiello A, eds, *Computer Vision–ECCV 2020*. Cham: Springer; 2020:251-266.

54. Shorten C, Khoshgoftaar TM. A survey on image data augmentation for deep learning. *J Big Data*. 2019;6:1-48.

55. Castro E, Cardoso JS, Pereira JC. Elastic deformations for data augmentation in breast cancer mass detection. *2018 IEEE EMBS International Conference on Biomedical & Health Informatics*. Las Vegas, NV, USA, 2018:230-234.

56. Spaide RF, Fujimoto JG, Waheed NK, Sadda SR, Staurenghi G. Optical coherence tomography angiography. *Prog Retin Eye Res*. 2018;64:1-55.

57. Bar-Kochba E, Toyjanova J, Andrews E, Kim K-S, Franck C. A fast iterative digital volume correlation algorithm for large deformations. *Exp Mech*. 2015;55:261-274.

58. Rister B, Horowitz MA, Rubin DL. Volumetric image registration from invariant keypoints. *IEEE Trans Image Process*. 2017;26:4900-4910.

59. Myronenko A, Song X. Point set registration: Coherent point drift. *IEEE Trans Pattern Anal Mach Intell*. 2010;32:2262-2275.

60. Hepp K. On listing's law. *Commun Math Phys*. 1990;132:285-292.

61. Chum O, Matas J. Optimal randomized ransac. *IEEE Trans Pattern Anal Mach Intell*. 2008;30:1472-1482.

62. Wang X, Beotra MR, Tun TA, et al. In vivo 3-dimensional strain mapping confirms large optic nerve head deformations following horizontal eye movements. *Invest Ophthalmol Vis Sci*. 2016;57:5825-5833.

63. Waldstein S, Faatz H, Szimacsek M, et al. Comparison of penetration depth in choroidal imaging using swept source vs spectral domain optical coherence tomography. *Eye*. 2015;29:409-415.

64. Ladd ME, Bachert P, Meyerspeer M, et al. Pros and cons of ultra-high-field MRI/MRS for human application. *Prog Nucl Magn Reson Spectrosc*. 2018;109:1-50.

65. Havsteen I, Ohlhues A, Madsen KH, et al. Are movement artifacts in magnetic resonance imaging a real problem?—a narrative review. *Front Neurol*. 2017;8:232.

66. Sim H, Oh J, Kim M. XVFI: Extreme video frame interpolation. *Proceedings of the IEEE/CVF Conference on Computer Vision and Pattern Recognition*, Montreal, Canada, 2021:14489-14498.

67. Gao W, Tedrake R. Filterreg: Robust and efficient probabilistic point-set registration using gaussian filter and twist parameterization. *Proceedings of the IEEE/CVF Conference on Computer Vision and Pattern Recognition*, Seoul, South Korea, 2019:11095-11104.

68. Grossman M. Parametric curve fitting. *Comput J*. 1971;14:169-172.

69. Lu J, Li Z, Bai J, Yu Q. Oriented and directional chamfer distance losses for 3D object reconstruction from a single image. *IEEE Access*. 2022;10:61631-61638.

70. Clark RA, Demer JL. Effect of aging on human rectus extraocular muscle paths demonstrated by magnetic resonance imaging. *Am J Ophthalmol*. 2002;134:872-878.

71. Sibony PA. Gaze evoked deformations of the peripapillary retina in papilledema and ischemic optic neuropathy. *Invest Ophthalmol Vis Sci*. 2016;57:4979-4987.

72. Sibony PA, Wei J, Sigal IA. Gaze-evoked deformations in optic nerve head drusen: Repetitive shearing as a potential factor in the visual and vascular complications. *Ophthalmology*. 2018;125:929-937.

73. Lee WJ, Kim YJ, Kim JH, et al. Changes in the optic nerve head induced by horizontal eye movements. *PLoS One*. 2018;13:e0204069.

74. Park J, Moon S, Lim S, Demer JL. Scanning laser ophthalmoscopy demonstrates disc and peripapillary strain during horizontal eye rotation in adults. *Am J Ophthalmol*. 2023;254:114-127.

75. Lim S, Tran A, Garcia SS, Demer JL. Optical coherence tomography angiography demonstrates strain and volume effects on optic disk and peripapillary vasculature caused by horizontal duction. *Curr Eye Res*. 2023;48:518-527.

76. Shin A, Yoo L, Park J, Demer JL. Finite element biomechanics of optic nerve sheath traction in adduction. *J Biomech Eng*. 2017;139:101010.

77. Park J, Shin A, Demer JL. Finite element modeling of effects of tissue property variation on human optic nerve tethering during adduction. *Sci Rep*. 2022;12:18985.

78. Chuangsuwanich T, Tun TA, Braeu FA, et al. Adduction induces large optic nerve head deformations in subjects with normal-tension glaucoma. *Br J Ophthalmol*. 2023. doi: 10.1136/bjo-2022-322461.

79. Lim S, Demer JL. Empirical quantification of optic nerve strain due to horizontal duction. *Bioengineering*. 2023;10:931.

80. Wang X, Chang S, Grinband J, et al. Optic nerve tortuosity and displacements during horizontal eye movements in healthy and highly myopic subjects. *Br J Ophthalmol*. 2022;106:1596-1602.

81. Eilaghi A, Flanagan JG, Simmons CA, Ethier CR. Effects of scleral stiffness properties on optic nerve head biomechanics. *Ann Biomed Eng*. 2010;38:1586-1592.

82. Erk KA, Henderson KJ, Shull KR. Strain stiffening in synthetic and biopolymer networks. *Biomacromolecules*. 2010;11:1358-1363.

83. Motte S, Kaufman LJ. Strain stiffening in collagen I networks. *Biopolymers*. 2013;99:35-46.

84. Le A, Shin A, Park J, Poukens V, Demer JL. Bilaminar structure of the human optic nerve sheath. *Curr Eye Res*. 2020;45:864-872.

85. Spaide R. Applications for oct enhanced depth imaging. The technology is providing previously unavailable insights into choroidal pathologies. *Retina Today Cover story*. 2011;1:57-59.

86. Coudrillier B, Tian J, Alexander S, et al. Biomechanics of the human posterior sclera: Age- and glaucoma-related changes measured using inflation testing. *Invest Ophthalmol Vis Sci*. 2012;53:1714-1728.

87. Park J, Shin A, Jafari S, Demer JL. Material properties and effect of preconditioning of human sclera, optic nerve, and optic nerve sheath. *Biomech Model Mechanobiol*. 2021;20:1353-1363.

88. Miller K. How to test very soft biological tissues in extension? *J Biomech Eng*. 2001;34:651-657.

89. Kim W, Argento A, Rozsa FW, Mallett K. Constitutive behavior of ocular tissues over a range of strain rates. *ASME J Biomech Eng*. 2012;134:061002.

90. Geraghty B, Jones SW, Rama P, Akhtar R, Elsheikh A. Age-related variations in the biomechanical properties of human sclera. *J Mech Behav Biomed Mater*. 2012;16:181-191.

91. Friberg TR, Lace JW. A comparison of the elastic properties of human choroid and sclera. *Exp Eye Res*. 1988;47:429-436.

92. Wollensak G, Spoerl E. Collagen crosslinking of human and porcine sclera. *J Cataract Refract Surg*. 2004;30:689-695.

93. Girard MJ, Downs JC, Bottlang M, Burgoyne CF, Suh J-KF. Peripapillary and posterior scleral mechanics—part II: Experimental and inverse finite element characterization. *ASME J Biomech Eng*. 2009;131:051012.

94. Elsheikh A, Geraghty B, Alhasso D, et al. Regional variation in the biomechanical properties of the human sclera. *Exp Eye Res*. 2010;90:624-633.

95. Pijanka JK, Spang MT, Sorensen T, et al. Depth-dependent changes in collagen organization in the human peripapillary sclera. *PLoS One*. 2015;10:e0118648.

96. Wale ME, Nesbitt DQ, Henderson BS, et al. Applying ASTM standards to tensile tests of musculoskeletal soft tissue: Methods to reduce grip failures and promote reproducibility. *J Biomech Eng*. 2021;143:011011.

97. Bekerman I, Gottlieb P, Vaiman M. Variations in eyeball diameters of the healthy adults. *J Ophthalmol*. 2014;2014:503645.

98. Demer JL, Clark RA. Translation and eccentric rotation in ocular motor modeling. *Prog Brain Res*. 2019;248:117-126.

99. Kapetanakis VV, Chan MP, Foster PJ, et al. Global variations and time trends in the prevalence of primary open angle glaucoma (POAG): A systematic review and meta-analysis. *Br J Ophthalmol*. 2016;100:86-93.

100. Kingman S. Glaucoma is second leading cause of blindness globally. *Bull World Health Organ*. 2004;82:887-888.

101. Shi D, Funayama T, Mashima Y, et al. Association of HK2 and NCK2 with normal tension glaucoma in the japanese population. *PLoS One*. 2013;8:e54115.

102. Iwase A, Suzuki Y, Araie M, et al. The prevalence of primary open-angle glaucoma in Japanese: The Tajimi study. *Ophthalmology*. 2004;111:1641-1648.

103. Kim C-s, Seong GJ, Lee N-h, et al. Prevalence of primary open-angle glaucoma in central South Korea: The Namil study. *Ophthalmology*. 2011;118:1024-1030.

104. Ha A, Kim YK, Jeoung JW, Kim DM, Park KH. Association of angle width with progression of normal-tension glaucoma: A minimum 7-year follow-up study. *JAMA Ophthalmol*. 2019;137:13-20.

105. Kim J-A, Kim T-W, Lee EJ, Girard MJ, Mari JM. Lamina cribrosa morphology in glaucomatous eyes with hemifield defect in a Korean population. *Ophthalmology*. 2019;126:692-701.

106. Killer H, Pircher A. Normal tension glaucoma: Review of current understanding and mechanisms of the pathogenesis. *Eye*. 2018;32:924-930.

107. Bonomi L, Marchini G, Marraffa M, et al. Prevalence of glaucoma and intraocular pressure distribution in a defined population: The Egna-Neumarkt study. *Ophthalmology*. 1998;105:209-215.

108. Klein BE, Klein R, Sponsel WE, et al. Prevalence of glaucoma: The Beaver Dam eye study. *Ophthalmology*. 1992;99:1499-1504.

109. Sommer A, Tielsch JM, Katz J, et al. Racial differences in the cause-specific prevalence of blindness in east Baltimore. *N Engl J Med*. 1991;325:1412-1417.

110. Rotchford AP, Johnson GJ. Glaucoma in Zulus: A population-based cross-sectional survey in a rural district in South Africa. *Arch Ophthalmol*. 2002;120:471-478.

111. Zhao J, Solano MM, Oldenburg CE, et al. Prevalence of normal-tension glaucoma in the Chinese population: A systematic review and meta-analysis. *Am J Ophthalmol*. 2019;199:101-110.

112. Seol BR, Kim S, Kim DM, et al. Influence of intraocular pressure reduction on progression of normal-tension glaucoma with myopic tilted disc and associated risk factors. *Jpn J Ophthalmol*. 2017;61:230-236.

113. Tseng VL, Kim CH, Romero PT, et al. Risk factors and long-term outcomes in patients with low intraocular pressure after trabeculectomy. *Ophthalmology*. 2017;124:1457-1465.

114. Siaudvytyte L, Januleviciene I, Ragauskas A, et al. Update in intracranial pressure evaluation methods and translaminar pressure gradient role in glaucoma. *Acta Ophthalmol*. 2015;93:9-15.

115. Jonas JB, Yang D, Wang N. Intracranial pressure and glaucoma. *J Glaucoma*. 2013;22:S13-S14.

116. Berdahl JP, Fautsch MP, Stinnett SS, Allingham RR. Intracranial pressure in primary open angle glaucoma, normal tension glaucoma, and ocular hypertension: A case–control study. *Invest Ophthalmol Vis Sci*. 2008;49:5412-5418.

117. Berdahl JP, Allingham RR. Intracranial pressure and glaucoma. *Curr Opin Ophthalmol*. 2010;21:106-111.

118. Gramer G, Weber BH, Gramer E. Migraine and vasospasm in glaucoma: Age-related evaluation of 2027 patients with glaucoma or ocular hypertension. *Invest Ophthalmol Vis Sci*. 2015;56:7999-8007.

119. Pircher A, Remonda L, Weinreb RN, Killer HE. Translaminar pressure in Caucasian normal tension glaucoma patients. *Acta Ophthalmol*. 2017;95:e524-e531.

120. Lindén C, Qvarlander S, Jóhannesson G, et al. Normal-tension glaucoma has normal intracranial pressure: A prospective study of intracranial pressure and intraocular pressure in different body positions. *Ophthalmology*. 2018;125:361-368.

121. Fortune B. Pulling and tugging on the retina: Mechanical impact of glaucoma beyond the optic nerve head. *Invest Ophthalmol Vis Sci*. 2019;60:26-35.

122. Wang YX, Jiang R, Wang NL, Xu L, Jonas JB. Acute peripapillary retinal pigment epithelium changes associated with acute intraocular pressure elevation. *Ophthalmology*. 2015;122:2022-2028.

123. Kim J-s, Kim YK, Kim YW, et al. Association between esodeviation and primary open-angle glaucoma: The 2010–2011 Korea national health and nutrition examination survey. *British Journal of Ophthalmology*. 2021;105:1672-1677.

124. Hong S, Yang H, Gardiner SK, et al. OCT optic nerve head morphology in myopia III: The exposed neural canal region in healthy eyes–implications for high myopia. *Am J Ophthalmol*. 2023. doi:10.1016/j.ajo.2023.08.012.

125. Wang B, Hua Y, Brazile BL, Yang B, Sigal IA. Collagen fiber interweaving is central to sclera stiffness. *Acta Biomater*. 2020;113:429-437.

126. Coudrillier B, Boote C, Quigley HA, Nguyen TD. Scleral anisotropy and its effects on the mechanical response of the optic nerve head. *Biomech Model Mechanobiol*. 2013;12:941-963.

127. Hötte GJ, Schaafsma PJ, Botha CP, Wielopolski PA, Simonsz HJ. Visualization of sliding and deformation of orbital fat during eye rotation. *Transl Vis Sci Technol*. 2016;5:9-9.

128. Schoemaker I, Hoefnagel PP, Mastenbroek TJ, et al. Elasticity, viscosity, and deformation of orbital fat. *Invest Ophthalmol Vis Sci*. 2006;47:4819-4826.

129. Zhang L, Beotra MR, Baskaran M, et al. In vivo measurements of prelamina and lamina cribrosa biomechanical properties in humans. *Invest Ophthalmol Vis Sci*. 2020;61:27-27.

130. Agar A, Li S, Agarwal N, Coroneo MT, Hill MA. Retinal ganglion cell line apoptosis induced by hydrostatic pressure. *Brain Res*. 2006;1086:191-200.

131. Friemel T, Grillo S, Stella Jr SL. Activation of Piezo1 mechanosensitive channels in retinal ganglion cells leads to cell death. *FASEB J*. 2020;34:1-1.

132. Maul TM, Chew DW, Nieponice A, Vorp DA. Mechanical stimuli differentially control stem cell behavior: Morphology, proliferation, and differentiation. *Biomech Model Mechanobiol*. 2011;10:939-953.

133. Hammerschmidt S, Kuhn H, Grasenack T, Gessner C, Wirtz H. Apoptosis and necrosis induced by cyclic mechanical stretching in alveolar type II cells. *Am J Respir Cell Mol Biol*. 2004;30:396-402.

134. Stavenschi E, Labour M-N, Hoey DA. Oscillatory fluid flow induces the osteogenic lineage commitment of mesenchymal stem cells: The effect of shear stress magnitude, frequency, and duration. *J Biomech*. 2017;55:99-106.